

AD-A141 096

MATHEMATICAL MODELLING OF LASER/MATERIAL INTERACTIONS

1/1

(U) IMPERIAL COLL OF SCIENCE AND TECHNOLOGY LONDON

(ENGLAND) DEPT... W M STEEN ET AL. 25 NOV 83

UNCLASSIFIED

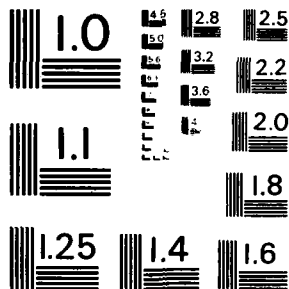
EOARD-TR-84-18 AFOSR-82-0076

F/O 12/1

NL

END  
DATE  
FILMED  
7-84  
DTIC

END  
DATE  
FILMED  
7-84  
DTIC



MICROCOPY RESOLUTION TEST CHART  
NATIONAL BUREAU OF STANDARDS-1963-A

FORM-TP-84-16

Contract/Grant No.

AFOSR - 82 - 0076

MATHEMATICAL MODELLING OF LASER/MATERIAL INTERACTIONS.

AD-A141 096

William M. Steen  
Metallurgy and Material Science Dept.  
Imperial College of Science & Technology  
London SW7 2BZ.

Jyoti Mazumder.  
Department of Mechanical Engineering  
University of Illinois  
Urbana  
Illinois  
USA.

25th November 1983.

Final Report 1st January, 1982 - 1st November 1983.

Approved for public release

Prepared for Air Force Office of Scientific Research. (AFSC) USAF.

and

EUROPEAN OFFICE OF AEROSPACE RESEARCH AND DEVELOPMENT, London, England.

DTIC FILE COPY

STIC  
MAY 16 1984  
A

EOARD TR-84-16

8 May 1984


This report has been reviewed by the EOARD Information Office and is releasable to the National Technical Information Service (NTIS). At NTIS it will be releasable to the general public, including foreign nationals.

This technical report has been reviewed and is approved for publication.



JOHN G. GOWAN  
Major, USAF  
Chief, Materials & Chemistry

FOR THE COMMANDER



JERRY R. BETTIS  
Lt Colonel, USAF  
Deputy Commander

REPORT DOCUMENTATION PAGE		READ INSTRUCTIONS BEFORE COMPLETING FORM
1. REPORT NUMBER <b>EOARD-TR-84-16</b>	2. G.O.T. ACCESSION NO. <b>A141 096</b>	3. RECIPIENT'S CATALOG NUMBER
4. TITLE (and Subtitle)  <b>MATHEMATICAL MODELLING OF LASER/ MATERIAL INTERACTIONS.</b>		5. TYPE OF REPORT & PERIOD COVERED  <b>FINAL 1/1/82-1/11/83.</b>
		6. PERFORMING ORG. REPORT NUMBER
7. AUTHOR(s)  <b>William M. Steen Jyoti Mazumder (Illinois Univ. Urbana).</b>		8. CONTRACT OR GRANT NUMBER(s)  <b>AFOSR - 82 - 0076</b>
9. PERFORMING ORGANIZATION NAME AND ADDRESS  <b>Imperial College of Science &amp; Technology, Metallurgy &amp; Materials Science Dept. London SW7</b>		10. PROGRAM ELEMENT, PROJECT, TASK AREA & WORK UNIT NUMBERS  <b>61102F 2301/D1</b>
11. CONTROLLING OFFICE NAME AND ADDRESS  <b>European Office Aerospace Research and Development LNS, BOX 14, FPO New York, 09510.</b>		12. REPORT DATE  <b>1st December 1983.</b>
		13. NUMBER OF PAGES
14. MONITORING AGENCY NAME & ADDRESS (if different from Controlling Office)  <b>EOARD/LNS Box 14 FPO New York 09510.</b>		15. SECURITY CLASS. (of this report)
		15a. DECLASSIFICATION/DOWNGRADING SCHEDULE
16. DISTRIBUTION STATEMENT (of this Report)  <b>Approved for public release, distribution unlimited.</b>		
17. DISTRIBUTION STATEMENT (of the abstract entered in Block 20, if different from Report)		
18. SUPPLEMENTARY NOTES		
19. KEY WORDS (Continue on reverse side if necessary and identify by block number)  <b>MATHEMATICAL MODELLING LASER WELDING RAPID SOLIDIFICATION HEAT TREATMENT CLADDING.</b>		
20. ABSTRACT (Continue on reverse side if necessary and identify by block number)  <b>The development of a detailed finite difference model of laser/material heat transfer is described. The model allows for thermal conduction, surface convection and radiation, variation in thermal properties, latent heat, keyhole formation and has some allowance for convection in the melt pool. It accounts for plasma interference but does not discuss the physical mechanisms involved within a keyhole. Some applications are described.</b>		

Mathematical Modelling of Laser/Material Interaction.

preface.

Dr Mazumder and Steen collaborated at Imperial College during the period 1975-79 when they developed the first finite difference models for heat transfer from a laser. There were two basic models developed that for a stationary beam (ref 1) and that for a moving beam (ref 2).

The predictive power of the moving beam model was soon appreciated and found to be useful in helping with the analysis of laser material processes such as arc augmented laser welding (ref 3) and laser welding (ref 4).

Mazumder moved to the States and although both authors continued to collaborate the distance between them was a physical disadvantage. This obstacle was partly removed by the help of this grant. As a result the moving beam model has been greatly refined as described in this report. The authors would like to acknowledge the help of the students in their two research groups but in particular. T. Chande (Illinois). P. Henry (ICST) K. Lipscombe (ICST), M. Sharp (ICST). They would also like to thank the USAF for enabling a useful cross fertilisation of these two active research schools one in USA one in UK.



## Introduction.

The finite difference model on which this work is based is fully described in ref 2.

The objective of this programme was to develop this model and use it. Thus this report falls into two parts. Firstly, aspects of the development of the model to allow for:

1. Latent heat effects.
2. Surface reflectivity variations
3. Mode structure
4. Variable thermal properties
5. Keyholing
6. Fluid flow in melt zone.

as well as the perpetual problem of speeding up convergence.

Secondly analysis of process performance illustrated by the model which can not be seen experimentally because variables can not be isolated, or in some cases even measured.

## 2. Model Development.

### 2.1 Latent Heat Effects

In general latent heat is absorbed in a leading location of the melt pool and released in trailing location. Thus the overall heat balance is unaffected by the presence or absence of latent heat. However, the exact melt pool shape is expected to be affected. In fact a longer melt pool should result from allowing for latent heat. Any variation in melt pool shape has a profound effect on cooling rates, solidification rates, and thermal gradients. These variables, in turn, describe the solidification mechanism and hence affect the weld metallurgy. Thus to allow for the latent heat is important.

Several algorithms were tried both at Illinois and London. The three algorithms which were most successful were based on a variable specific heat.

One has an artificially high specific heat function during the assumed melting and boiling temperature bands (described in appendix A).

The function was:

$$C_p(T) = C_{p_0} + \Delta H / \Delta T_m \quad \text{from } T_m \leq T \leq T_m + \Delta T_m$$

$$C_p(T) = C_{p_0} + \Delta H_v / \Delta T_v \quad \text{from } T_v \leq T \leq T_v + \Delta T_v$$

where

$$C_{p_0} = \text{the normal constant specific heat J/kg } ^\circ\text{C}$$

$$\Delta H_v, \Delta H_m = \text{Transition energies - latent heat J/kg}$$

$$\Delta T_m, \Delta T_v = \text{Temperature band over which transition occurs } ^\circ\text{C}$$

although this model was felt to have good physical justification it predicted lengthy melt pools (8mm for a 2kW laser power). The recovery of all the latent heat of vaporisation in the trailing edge of the pool was considered to be the cause. Improved versions of the model which ignore the recovery of the latent heat of vaporisation gave reasonable melt pool lengths.

Another latent heat algorithm was to have a numerical hold for a set number of iterations before passing the transition temperature. This has an analogy with the temperature rise of a single point. For the quasi steady state solution sort it had little effect on the answer compared to the model without this algorithm

A third algorithm used was to have an artificial linear variation of specific heat with temperature to accommodate the latent heats over an extended temperature range. For example:-

$$\bar{C}_p \Delta T_m = \int_{T_0}^{T_m} C_p dT + L$$

where  $\Delta T_m = (T_m - T_0)$  and  $\bar{C}_p =$  the specific heat

used in that interval. (described in appendix B).



This third model gave the best convergence. The first model had instabilities due to the step change in specific heat. The first and third models both had reasonable predictive power.

This aspect of the work is written up in "Modelling Laser Heating Effects" by P. Henry et al. (appendix A) and "Estimating Effects of processing conditions and variable properties on pool shape, cooling rates, and absorption coefficient in laser welding" by T. Chande et al (appendix B)

## 2.2 Surface reflectivity variation.

The complexity in modelling laser interactions is the intimate interrelationship of the variables concerned. This not only means experimentation is so complex that a real understanding can only be found through mathematical analysis but also that in building the model it is difficult to verify the result. The variation of surface reflectivity with temperature, phase and surface shape, and gas plasma effects is such an example. Hard experimental data at high temperatures are not available and if obtained of doubtful value due to the strong variations possible with such localised events as surface deformation (including keyholing) and plasma generation. Thus any algorithm is produced against a blank background of experience. It is known that the material property of reflectivity (as opposed to the surface property of reflectance) falls with rise in temperature due to the lattice phonons and atomic vibration states being more available for absorption to electromagnetic radiation. However the reflectance experienced by the beam is made up of the material property reflectivity and a shape factor. The shape, in the form of roughness, or melt depressions, may be such as to cause a single ray to be reflected twice or more before leaving the surface. In consequence greatly reducing the surface reflectance. This geometric factor is not temperature dependent and it may be the dominant term; for example the reflectivity of aluminium to 10.6  $\mu$ m radiation is around 96% shot peened aluminium has a reflectance of around 50%.

The gaseous absorption in laser generated plasmas becomes significant at gas temperature of  $7000^{\circ}\text{C}$  (Saha Equation ). This factor is highly temperature dependent. The chosen algorithm needs to be responsive to these main features of the surface reflectivity. Several algorithms were chosen. Firstly a constant reflectivity up to the boiling point after which it was zero - due to the formation of a blackbody keyhole. As in the case of latent heat modelling this step function contributed to instabilities.

Secondly a constant reflectivity was assumed up to a temperature  $T_1$ , it then steadily fell to temperature  $T_2$  after which it was zero.

Using the first model fig. 10 of appendix B shows how insensitive the weld pool is to the surface reflectivity provided it is low enough to allow boiling. Once boiling occurs the power absorbed in the keyhole totally dominates the process.

Using model 2 with  $T_1 = T_B/2$   $T_2 = T_B$  the same effect is noticed where  $T_B = \text{Boiling Point}$ .

### 2.3 Mode Structure.

Considerable debate within laser manufacturing circles is centered on the significance of mode structure. A Gaussian beam is known to focus to the finer spot defined by diffraction limited optics as:

$$d_{\min} = 2.4f\lambda/D$$

where

f	= Focal length of lens	mm
$\lambda$	= Wavelength of light used	mm
D	= Incident beam diameter on lens	mm
$d_{\min}$	= Minimum focal spot size	mm

In practice this is never achieved because of finite aperture in laser cavities and off axis oscillation states known as TEM<sub>m</sub>n mode (transverse electromagnetic modes). Thus different lasers have different limiting spot sizes for given focal length lenses and spherical aberration

$$d_{\min} = 2.4 (m + 1) f\lambda/D$$

where m is a mode factor (usually around 4)

The model can accommodate any defined surface power distribution expressed as the average power over the finite elemental areas. Thus an equation for the power distribution P (r,θ) or P(x,y) is easily translated to the model input. Even an experimental mode print can also be digitalised for the model. In trying to describe high order modes mathematically a problem is immediately found. It is the definition of beam diameter. The characteristic radius found in mathematical representations of various oscillation modes (eg ref.5) is a function of the laser cavity alone and is therefore independent of mode structure. What is required for material processing is the radius within which  $(1 - e^{-2})$  of the power falls - this factor makes the beam radius equal to the radius for a Gaussian beam out to the point where the power has fallen to  $1/e^2$  of the central value.

Thus the spot size was defined as: 
$$\int_0^R \int_0^{2\pi} P(r, \theta) r dr d\theta = (1 - e^{-2}) P_t$$

Where  $P_t$  = total incident power W  
 $P(r, \theta)$  = intensity distribution W/cm<sup>2</sup>  
 $r, \theta$  = cylindrical coordinates

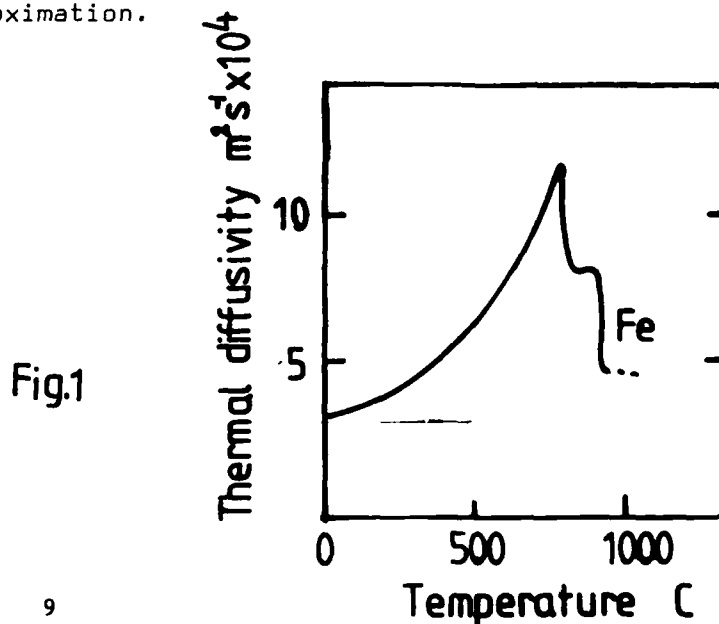
and a mode factor K defined to relate the processing radius R to the characteristic radius of a Gaussian beam, w

$$R = Kw$$

This particular work is described in appendix C. "An analysis of the effect of Mode Structure on laser material Processing" by M. Sharp et al.

#### 2.4 Variable Thermal Properties.

The thermal properties describing the flow of heat in a solid are the thermal conductivity, specific heat, and density. Together they define the thermal diffusivity. The original model in common with most models assumed constant values for these properties. However, this variation with temperature in most metals is by no means insignificant. Swifhook & Gick (ref.5) used average values over the temperature range considered, but reference to fig.1 below and fig.1,2,3 of appendix B shows this can only be a convenience rather than an allowable approximation.



The thermal properties of the liquid phase are even more difficult to define due to the strong convection forces within the molten pool. (see appendix D) as well as the lack of hard data.

In the model an enhanced thermal conductivity of the melt pool is assumed to allow for convection.

In one version of the model (see appendix B) the individual grid volumes are given thermal properties by the elements temperature.

According to the algorithm below:

$$\begin{aligned} K &= A + BT + CT^2 \quad \text{or } AT^n \\ C_p &= AT^n \end{aligned}$$

## 2.4 Keyholing

By defining a grid element to have boiled away if it exceeds the boiling point to allow the radiation to fall on the element beneath it, a keyhole can be computed. This simple model means if keyholing starts then the depth of penetration is very large. Infact for certain power densities it would be infinite if the power is sufficient to boil an element with the surrounding elements cold. This is not the case in reality so the model had to include some factor to limit the penetration depth. In reality the penetration depth is probably kerbed by either plasma absorption or keyhole instability - that is the liquid walls flowing downwards. Experimentally it has so far been impossible to seperate these two possible mechanisms.

In the model a plasma absorption mechanism was assumed such that the radiant intensity falling on the element distance  $Z$  from the surface after the elements above it have boiled away, is defined by a Beer-Lambert relationship.

$$P_2 = P_s \exp(-\beta Z)$$

where  $P_2$  = Power density at depth  $Z$   $W/m^2$

$P_s$  = Surface power density  $W/m^2$

$\beta$  = Beer-Lambert coefficient  $m^{-1}$

The problem now shifted to the value  $\beta$  and its variation with temperature. The absorption of plasma for steel is given by Yamanawa and others but the values are hard to use since distances were not known. It is however possible to evaluate  $\beta$ , assuming it has a constant value, from penetration data. Alexander ref. 6 found a slight plateau in weld penetration depth vs speed. Using this plateau penetration the following values of  $\beta$  were derived.

(ref 3 Steen) by assuming the surface energy at the

Power W	Depth mm	$\beta$ m <sup>-1</sup>	Power at base Keyhole W
1300	2.3	700	260
1500	2.4	700	260
1700	2.72	700	256

base of the keyhole, which is zero reflection, was the same as the energy required to start the keyhole against the surface reflectivity.

The Beer-Lambert coefficient is a sensitive processing parameter as illustrated in appendix B fig. 9. Possibly the only way a hard value can be found for it is by comparing the model with fusion profiles. This would be a dangerously circular way of finding the value of  $\beta$  and proving the model's validity. Convergence is a difficulty when keyholing is operating. There tends to be a thermal vibration on certain grid elements. There does not appear to be any instability in the heat transfer equations.

The problem appears to be associated with the very high power input into the vaporised elements and the element below. The vaporised elements are kept at artificially high temperatures in the conduction matrix. This and the lack of any sophistication in power distribution within the keyhole by wave guiding is currently forming one area of further development.

The modelling of a keyhole forming is illustrated in fig.1 of appendix A.

### 2.6 Fluid Flow in the Melt Zone.

The flow within the melt pool would stimulate heat flow and hence behave as an augmentation of the thermal conductivity. It differs from the thermal conductivity in that it is not a scalar property. However, in the laser interaction zone the flow is driven by a surface tension force operating in the direction of maximum thermal gradient, and thus on the surface the flow vector is parallel to the thermal flow vector. Beneath the surface this is unlikely to be the case.

The best mathematical model would incorporate a flow analysis via the Navier-Stokes equations. Such analysis would increase the storage requirements for computing and the computing time. However, a start was made on this complex problem as discussed in appendix D.

For the thermal model an arbitrary increase in thermal conductivity was tried. The algorithm was:

$$k^1 = m(k)$$

where  $m = 2$  or  $3$  for Al  
 $4$  or  $5$  for Fe

The effect of this modification was negligible. This is probably because an increase in conductivity of the melt pool only should increase the melt pool temperature and hence size but the consequent increased gradient over the outer area of the pool undersurface would have the opposite effect.

### 2.7 Convergence.

The original model had an exponential grid pattern (ref.1). This led to difficulties in defining power inputs correctly and the temperatures of elements. It was believed that mismatches of temperatures and powers led to mathematical lack of focus in the model and hence some instability. Convergence with a uniform grid was comparatively swift but the boundary conditions were less assured.

For example the edge boundary condition was assumed to be:

$$\left(\frac{dT}{dx}\right)_{\text{edge}} = 0 \quad ; \quad \left(\frac{dT}{dy}\right)_{\text{edge}} = 0$$

Thus the model was arranged to cycle a fixed number of times ( $\sim 50$ ) with an exponential grid and then redefined to a uniform grid up to the limits of convergence. The removal from the model of step function algorithms as far as possible also contributed to stability.

Typical computing times are:- 1500 iterations in 11 min 55 sec.  
CDC/Cyber 174.



### 3. Application of the Model.

The model produces an answer which is the temperature matrix for the quasi steady state profile beneath the laser beam. This thermal matrix is moving through the material at the traverse speed.

Thus this data needs adapting to whatever application is considered.

The usual parameters calculated from the model are.

- a. Boundaries of specific isotherms - eg fusion boundary, or  $Ac_3$  boundary.
- b. Boundaries for regions above a certain temperature for longer than a certain time.
- c. Thermal gradients
- d. Solidification rates
- e. Cooling rates.

#### 3.1 Isotherm boundary applications.

One of the earliest applications was in the evaluation of the role of the electric arc in arc augmented laser welding by Eboo et al (ref 3,7) and theoretical welding speeds by Mazumder et al (ref 4,8) and appendix A fig 10,11,12,13. Currently appendix B shows the more intraverted applications of assessing the significance of the variation of parameters which are impossible to experiment with such as  $\beta$ ; reflectivity, thermal conductivity (fig 9,10, 11 appendix B).

The experimental determination of depth of hardness was originally attempted by Courtney et al (ref 9) in which the parameter  $\left[ \frac{P}{\sqrt{DV}} \right]$

where

P	=	Power W
D	=	Incident spot size m
V	=	Traverse speed m/s.

was found to be proportional to the depth of hardness when there was no surface melting. Analytic studies using the model are discussed in appendix A.

Fig 14,15 appendix A show that this experimentally observed linearity is only approximately true, the beam diameter behaves in a more complex manner but not one causing sufficient variations to be noticed from the normal experimental noise.

In appendix A the weld penetration is calculated for large unfocussed spots because this falls in the region of rapid solidification or surface alloying. These laser processes are currently attracting considerable attention and the model is capable of reasonably accurate melt pool size predictions. But it must be remembered that precise reflectivity and beam sizes are not known in practice.

### 3.2 Thermal gradient and cooling rate application.

In these processes, as well as welding, the solidification structure is very important. The fineness of the solidified structure (eg dendrite arm spacing) is found to be inversely proportional to the cooling rate (G.R) (thermal gradient  $G$   $^{\circ}\text{C}/\text{m}$  x solidification rate  $R$   $\text{m/s}$ ) and for eutectic growth  $\lambda R = \text{const}$  where  $\lambda$  = plate spacing,  $\text{m}$ . The solidification mechanism (planar, cellular, dendritic) is described by the tendency to constitutional supercooling which is defined by the parameters  $(G/R)$ . The phases which crystallise or undergo solid state transformation are decided by thermodynamics and kinetics. During rapid quenching supercooling is normal, this can affect which phases are favoured thermodynamically.

What actually occurs is determined by the nucleation and growth mechanisms in the melt. In this respect the crystals at the base of the melt represent nuclei encouraging epitaxial growth while at the same time undergoing grain growth. This extremely complex interaction of events in a moving melt pool is difficult to describe by the data from the model. The cooling rate  $G.R$  and some extra

data such as a III curve for the alloy considered are currently the best analysis possible, some initial studies involving the basic kinetic and nucleation parameters have been made by Bergman (ref 10). Whatever eventually matures in this area the thermal gradient  $G$  and the solidification rate  $R$  are almost certain to be required.

The scale and extent of segregation in the weld metal would be expected to be determined by the concentration "bow wave" ahead of the solidifying front which if governed solely by diffusion in the melt can be described by

$$X_s = X_0 \left\{ 1 - \frac{1-k}{k} \exp\left(-\frac{x}{D/R}\right) \right\}$$

where

- $k$  = partitioning coefficient =  $X_{\text{solid}} / X_{\text{liquid}}$
- $X$  = concentration
- $D$  = solute diffusivity in the melt  $\text{m}^2/\text{s}$
- $R$  = rate of solidification  $\text{m/s}$
- $x$  = distance from solidifying front  $\text{m}$

Thus a knowledge of  $R$  would allow some semi quantitative analysis of segregation.

Cooling rates  $G.R.$  are discussed in appendix A, B, and E  
In appendix E "Range of rapid solidification structures with laser surface treatment of special steels" by G. Christodoulou, P. Henry, W.M. Steen Proc 4th Int. Conf on rapidly quenched metals (Sendai 1981).

Graphs are shown of  $G.R.$  and  $G/R$  contours in a keyhole weld.

In appendix B an advance is made by identifying a dimensionless melt front velocity  $\emptyset$  where  $\emptyset = (P/d^2) / (\mu \rho C_p \Delta T_m)$

This is a psuedo melting efficiency. This group may prove to be a useful parameter for collating the data obtained from each run.

Dimensionless operating parameters which allow generalised results to be expressed is the next step in the application of this model.

Attempts to apply the model to other processes than welding are underway. Appendix F shows the coupling of the thermal conduction model to a variable surface shape and power distribution to simulate laser pneumatic cladding.

The success of this is quite striking (eg fig 11 appendix F)

## CONCLUSIONS.

A sophisticated finite difference model has been developed capable of taking account of surface variations in convection, radiation and reflectivity bulk variations in thermal conductivity, density and specific heat and Physical events such as phase transformations involving latent heat keyhole formation, plasma absorption and flow in the melt pool.

The computing time is reasonable for a large mainframe computer.

Applications of the model are currently centred on calculating thermal gradients,  $G$ , solidification rates,  $R$ , and locations of specified isotherms for processes such as surface melting and welding. It has also been adapted to model clad thickness and rate of deposition as well as  $G$ ,  $R$ , and isotherm locations for the process of laser cladding with blown powder feed.

REFERENCES.

1. Steen W.M., "The thermal History of a spot heated by a laser" Letters Heat & Mass Transfer Vol 4 pp 167 - 178 1977
2. Mazumder J. Steen W.M. "Heat Transfer model for CW Laser Material Processing" J. App Phys 51 (2) Feb 1980 p 941 - 947
3. Steen W.M. "Arc augmented laser processing of materials" J. App. Phys, 51 (11) Nov 1980 pp 5636 - 5641
4. Mazumder J. Steen W.M. "Welding of Ti 6al - 4V by continuous wave CO<sub>2</sub> laser". Metal construction Sept. 1980 pp423 - 427.
5. Kogelnik H, Li.T Proc IEEE 54 1312 1966
6. Alexander J. "Penetration studies in laser and arc augmented laser welding" Ph.D London Univ. Feb 1982.
7. Eboo. M. "Arc augmented laser welding" Ph.D Thesis, London University, March 1979
8. Mazumder J. "The laser welding of Ti and tin plate" Ph.D Thesis London University April 1978
9. Steen. W.M., Courtney C. "Surface hardening of EN8 Steel with a laser" Metals Tech. Dec 1979 p 456 - 462
10. Bergman. H. H.U. Fritch, Calculation and calorimetric measurement of crystallisation behaviour of metallic glasses. (Tech Inst, Clausthal, W. Germany).

REFERENCES.

- A. Henry P. Chande. T., Lipscombe K, Mazumder. J, Steen W.M.  
"Modelling Laser Heating Effects" paper 4B-2  
ICALEO '82 conf. Boston Sept. 1982.
- B. Chande. T., Mazumder. J. "Estimating effects of processing  
conditions and variable properties upon pool shape, cooling  
rates and absorbtion coefficient in laser welding" submitted  
to J. app. Phys
- C. Sharp M. Steen W.M. Henry. P., Lim. G.C. "An analysis of the  
effect of mode structure on laser material processing" Laser  
'83. Opto Electronik conf. Munich 1983 to be published.
- D Chan. C. Mazumder J. Chen. MM "A two dimensional transient model  
for convection in laser pools" ICALEO Conf. Boston 1982.
- E. Christodoulou G. Henry. P., Steen W.M. "Range of rapid  
solidification structures with laser surface treatment  
of special steels" Proc. 4th Int. conf. on rapidly quenched  
metsls Sendai, 1981.
- F. Weerasinghe. V.M., Steen W.M. "Computer simulation model for  
laser cladding" ASM meeting. Boston Nov 1983.

LASER HEATING THEORY

P. Henry\*, T. Chande\*, K. Lipscombe\*, J. Mazumder\*, W.M. Steen\*

\*Mechanical Engineering Dept., University of Illinois  
Urbana, Illinois, U.S.A.

\*Metallurgy Dept., Imperial College, London SW7 2BP  
U.K.

ABSTRACT

The results shown here are some preliminary studies in the co-operative development of a 3D finite difference model of the laser heating process. Two models are currently under investigation that derived at Imperial College and that at the University of Illinois. They have a similar root in the original work of Mazumder and Steen (1).

Reported here are some results of the working of the model. These illustrate amongst other things the flexibility of this form of calculation and our ability to discuss the importance of latent heat, variable reflectivity, variable thermal properties and keyholing.

INTRODUCTION

Laser irradiation produces rapid local heating in metallic substrates, this can be followed by high cooling rates when irradiation is stopped or withdrawn due to conduction into the substrate. Metallurgically attractive surface structures can thus be readily generated.

Laser material processing involves complex physical processes and interactions that would require considerable experimental effort to understand. A mathematical model offers a powerful addition to an otherwise purely experimental approach when it comes to resolving these problems.

Analytical mathematical models are limited by the assumptions necessary to make the problem tractable. Numerical models can be more general and can be made to allow for non-linear surface events, such as radiation losses, or variable absorption due to surface evaporation as in "keyholing". They can also be made to accommodate variations in the power distribution across the laser beam (mode structure) as well as variations in the substrate optical and physical properties due to temperature dependence.

A number of numerical models of laser/material heating have been suggested. The simple one dimensional heat flow model of Kear et al (2), has its attractions since the answers can be displayed in a fairly generalised form, as for the spot heating solution of Ready (3).

More sophisticated three dimensional models are less easy to express as generalised solutions. Kou et al (4) derive a model based on an oblate spheroidal coordinate system which is converged by a Gauss Siedel iteration method. Since this coordinate pattern would be expected to fit the isotherms better than the orthogonal system discussed here, it should achieve a more accurate solution faster. However, it appears that Kou's method involves a considerable computing penalty, and is not yet able to account for keyholing and surface heat losses.

The model described here allows for surface heat losses by radiation or convection, variable thermal properties, and reflectivity as well as latent heat effects and "keyholing".

There are so many variables that dimensional analysis does not significantly simplify the presentation of the solutions. Thus the working of the models is illustrated here by examples of particular laser/material interactions.

DESCRIPTION OF MODELS

In this project two models for laser material processing were compared. They are both based on a 3D numerical finite difference model described elsewhere by Mazumder and Steen (1).

The original root form had an exponential grid to remove the boundaries so that they had effectively no thermal gradient across them. The Illinois model introduced a two stage grid setting, starting with an exponential grid to roughly find the heated zone and



then dividing this smaller zone into a regular grid. Such a system greatly reduces the convergence time. They also introduced variable thermal properties and reflectivity and the form of the form:

$$V(T) = a + bT + c/T$$

where  $V(T)$  is some property (eg thermal diffusivity)

$T$  is temperature

$a, b, c$  are constants.

Meanwhile the Imperial College version had been adapted by Iboo (5) to allow for keyholing and plasma absorption effects. They also tried variable reflectivity in linear step functions.

Naturally as improvements were developed in either place they were incorporated into the versions. Currently the analysis is focussed upon latent heat effects. The Imperial model attempts to allow for this by introducing a hold in the interaction of the relaxation method as transition temperatures are encountered.

The Imperial model has been adapted to have a modified specific heat function, which uses an artificially high specific heat during the assumed melting and boiling bands. The function is

$$\text{and } \begin{aligned} \text{Cp}(T) &= \text{Cp}_0 + \Delta P/\Delta T_m \text{ from } T_m \leq T \leq T_m + \Delta T_m \\ \text{Cp}(T) &= \text{Cp}_0 + \Delta H_V/\Delta T_V \text{ from } T_V \leq T \leq (T_V + \Delta T_V) \end{aligned}$$

where  $\text{Cp}_0$  = the normal constant specific heat J/kg°C

$\Delta P_V, \Delta P_m$  transition energies, - latent heat J/kg

$\Delta T_m, \Delta T_V$  temperature band over which transition occurs °C

The effect of these differences and their physical significance forms the main area of cooperation work between the two centres. So far this cooperation has resulted in a model of increasing accuracy and sophistication with decreasing convergency times.

#### RESULTS

Fig. 1 shows cross sections of the melt pool for typical laser glazing runs on CPTi (Commercially Pure Titanium). The reflectivity in this run changed linearly from a value such as 0.7 down to zero at the melting point. The onset of keyholing can just be seen at the slower speed. In this figure latent heat was allowed for, similar shaped profiles are obtained if latent heat effects are ignored, however in these cases the melt pool and isotherm fields produced are wider and deeper across the track but shorter along it. Latent heat effects suppress the thermal penetration by introducing heat sinks which slow up the heating process and limit the peak temperatures and thermal gradients.

In figs. 2,3,4 the affects of increasing traverse speed on the melting (1960K), 1300K 1000K and 700K isotherms, is demonstrated. Keyholing is just apparent at the slower speed of 18 cm/s, but above this at 30 or 100 cm/s the melt pool is conduction limited with only surface absorption of the laser radiation. The 1000K isotherm roughly marks the extent of the HAZ (heat affected zone). There is a noticeably steeper gradient at the faster speeds. Figs 5 and 6 are views of the melt pool from above. The lines show the extent of the pool at depth intervals of

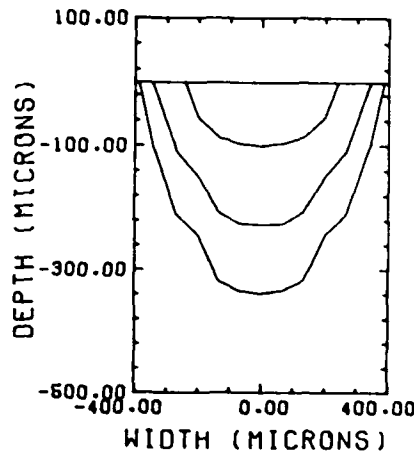


Fig. 1 Theoretical melt pool cross section in CP Titanium made with 2 kW laser power and a focussed 0.2 mm beam diameter at various speeds: 18, 30, 100 cm/s

100  $\mu\text{m}$  output such as this can yield some insight into the laser material interaction. The predictions agree fairly accurately with experiments in both width and depth of the fusion and HAZ, but the extent and shape of the melt pool are surprising. The effect of latent heat is to cause an energy absorption at the leading edge of the pool and an energy release at the trailing edge, thus extending the length of the pool. The results from the Illinois version which does not allow for latent heat by the quasi-specific heat method, but by the numerical hold method produces a shorter pool of around 1.5 mm for these parameters. It is possible to argue that the latent heat of vaporisation will be totally or partially lost to the system and not repaid at the trailing edge as is assumed here. It is also possible to argue that the reflectivity is only zero once boiling occurs and not once melting occurs, both of these arguments would produce a shortened weld pool and variations such as these are currently under development.

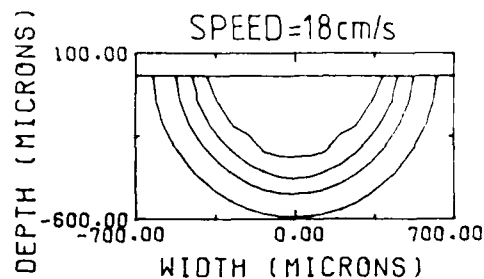


FIG 2

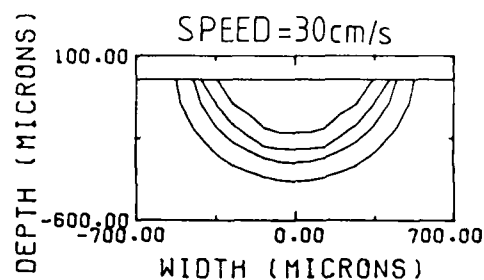


FIG 3

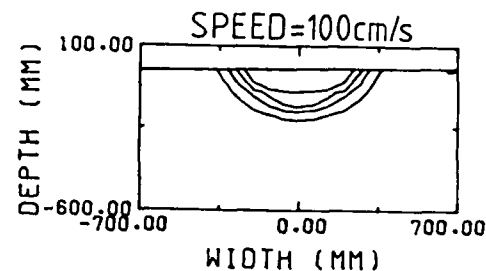


FIG 4

Fig. 2-4 The effect of increasing traverse speed on the 700°K, 1000°K, 1300°K, and 1960°K isotherms in CP Titanium using 2 kw laser power and 0.4 mm diameter beam size.

Fig. 5. View of melt pool from above showing contours at 100  $\mu\text{m}$  depth intervals: for 2 kw laser power; 0.4 mm spot size and 30 cm/s traverse speed.

Fig. 6. As for fig. 5 but at the slower speed of 18 cm/s

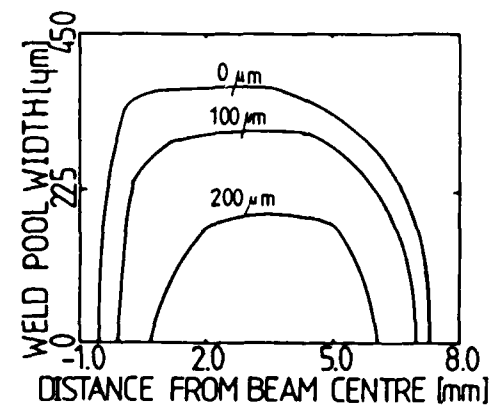


FIG 5

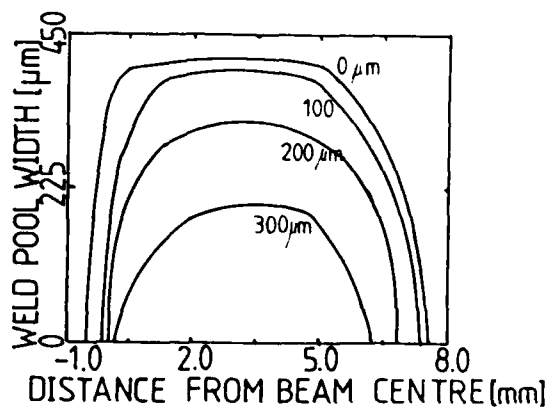


FIG 6

...the initial sub-second rise above the boiling point is the probable indication that there is some plasma heating which would create a "tail heard" to the weld pool. The region of solidification at the trailing edge shows a steep cooling rate of the order of  $10^6 - 10^8$  K/s in both cases, with the highest rates at the surface.

The "heat sink" affect of the latent heat is illustrated in Fig. 9 where Fig. 7 is transposed from temperature to temperature equivalent based on the enthalpy

$$T_{eq} = T + \frac{\sum Q}{Cp_0}$$

$Q$  = Any stored latent heat

It is seen here that the plateau region in the temperature profile is actually a region in which the latent heat of boiling is conducted out of the system. As argued previously this is probably not true physically and the latent heat of boiling is lost to the system by evaporation. Where allowance is made for this the plateau region of Figs. 7 and 8 would be considerably reduced.

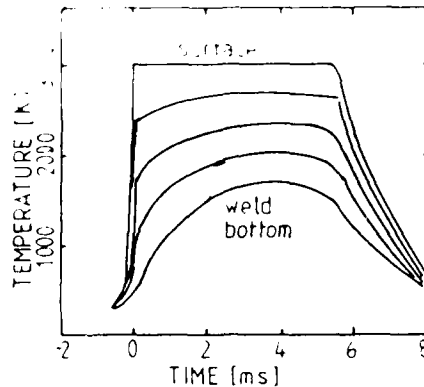
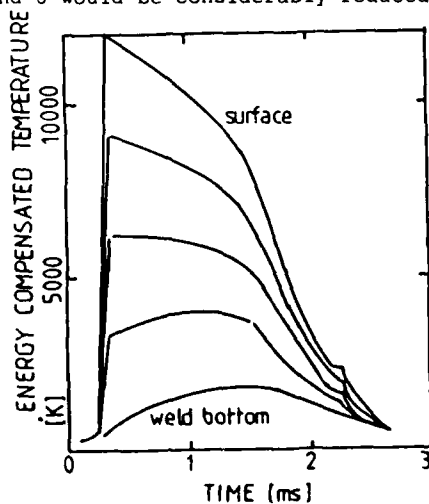


Fig. 7. Thermal history curves for points at different depths on the weld pool centre line. (Power (P) = 2kw; spot size (D) = 0.4mm; (speed (V) = 100 cm/s CP titanium.)

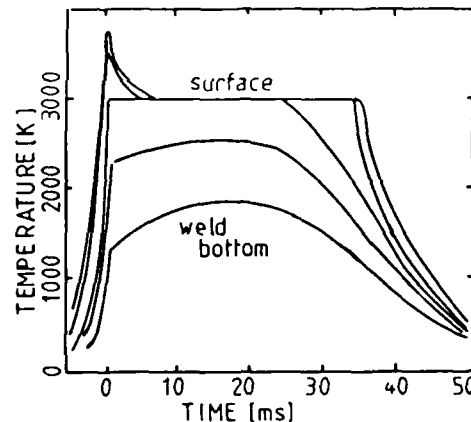


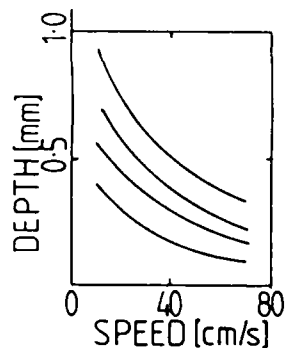
Fig. 8. As for fig. 7 but at the slower speed of 18cm/s

Fig. 9. Enthalpy - time curve of the data shown in fig.7.

A line graph showing the relationship between Depth [mm] (Y-axis) and SPEED [cm/s] (X-axis) for various temperatures. The Y-axis ranges from 0 to 0.8 mm, with a major tick at 0.4. The X-axis ranges from 0 to 100 cm/s, with major ticks at 0, 50, and 100. There are five curves, each representing a different temperature. All curves show a decreasing trend of depth with increasing speed. The curves are ordered by temperature, with the highest temperature curve (100°C) being the uppermost and the lowest temperature curve (20°C) being the lowermost.

SPEED [cm/s]	100°C Depth [mm]	60°C Depth [mm]	40°C Depth [mm]	20°C Depth [mm]
10	0.75	0.65	0.55	0.45
50	0.45	0.35	0.28	0.20
100	0.30	0.25	0.20	0.15

Fig. 13 describes the depth of heating when working with a large 3 mm diameter beam of 1 kW power. This is operating within the area for transformation hardening without surface melting. Fig. 13 shows that surface melting starts at traverse speed less than 12 cm/s for C.P. Titanium, at this speed the 700K (approx. eutectoid temperature) isotherm penetrates 0.3 mm, whereas with a 2mm beam diameter (Fig. 12) and 2 kW of power speeds in excess of 55 cm/s are required to suppress melting giving a 700K isotherm penetration depth



25

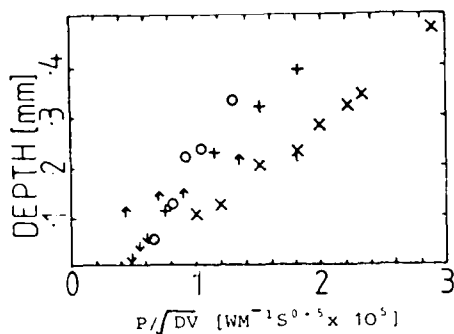


Fig. 14. A parametric plot of depth vs  $P/\sqrt{DV}$  for the penetration of the 1960°K melt isotherm. The symbols are for the following conditions:

	P	D	V
x	2kw	0.4mm	various
+	2kw	1.0mm	"
o	2kw	2.0mm	"
·	1kw	3.0mm	"
+	various	0.4mm	30cm/s

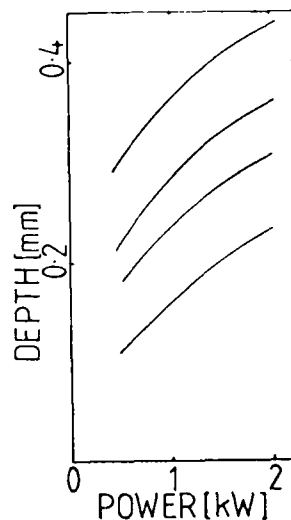


Fig. 15. Variation of penetration of the 700°K, 1000°K, 1300°K, and 1960°K isotherms with power ( $D = 0.4\text{mm}$ ,  $V = 30\text{cm/s}$ , CP titanium)

reduced to around 0.2 mm. It is thus possible to calculate the required operating curves of speed, power and beam diameter to achieve certain penetrations of specific isotherms in any materials of interest.

Experimentalists have tried to correlate penetration data against a variety of parameter groups such as specific energy ( $P/DV$ ), thermal penetration ( $P/\sqrt{DV}$ ) or even power density ( $P/D^2$ ). Fig. 14 shows the theoretical predictions of depth vs  $P/\sqrt{DV}$ . A nesting of the data is observed which if it had been experimental could be considered as a viable correlation within the bounds of experimental accuracy, theoretically we find a significant scatter to be present. The fit to  $1/\sqrt{V}$  is good but that for  $P/\sqrt{DV}$  is not so good. The reasoning for a possible correlation of depth of HAZ with  $P/\sqrt{DV}$  is based on the simplification that the variation in temperature with depth can be expressed in the form:

$$T^* = A''^* \text{ where } T^* = \pi k D / P \\ \text{and } \theta^* = \sqrt{4 \alpha t / x}$$

The heating time,  $t$ , is approximately given by the interaction time ( $D/V$ ) and thus:

$$\theta^* = \frac{1}{x} \sqrt{\frac{4 \alpha D}{V}}$$

substituting these terms into the dimensionless equation yields

$$\frac{T \pi k D}{P} = \frac{A}{x} \sqrt{\frac{4 \alpha D}{V}}$$

and hence for a given  $T_E$  depth of penetration  $x$  is

$$x = \frac{P}{\sqrt{DV}} \cdot \frac{4 \alpha}{T_E \pi k}$$

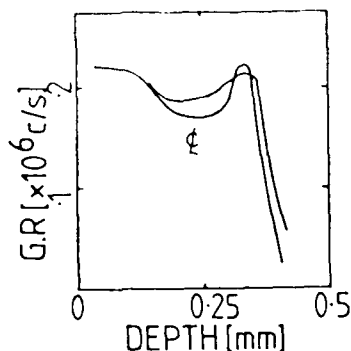


Fig. 16 The variation of cooling rate G.R with depth in a keyhole weld pool, for the centreline and a plane 1 mm to one side of the centreline. (P = 2kw, D = 0.4mm, V = 16cm/s)

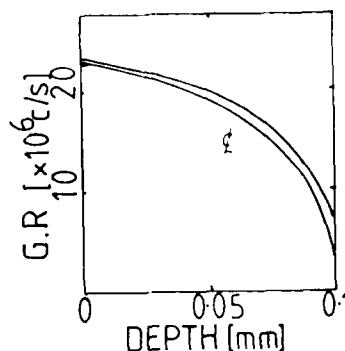


Fig. 17 As in fig. 16 but for a conduction limited weld pool. (P = 2kw, D = 0.4mm, V = 100 cm/s)

To fit the actual data a more refined model than equation (1) is being developed.

Fig. 15 shows the non-linear increase in depth of theoretical penetration with power. This is partly due to the temperature suppression with latent heat but principally is due to the rate of heat flow within a solid body being limited by the Fourier number, which is not power dependent.

Finally Figs. 16 & 17 illustrate the possibility of calculating important metallurgical parameters which cannot normally be measured. In this case the solidification interface cooling rate (G.R where G is solidification rate (m/s) and R is the thermal gradient K/s) which affects the scale of metallurgical microstructures is shown for the centreline and line adjacent to it (67  $\mu$ m to one side). The curves show the rise in cooling rate as the surface is approached as has been predicted by Kear et al.<sup>(2)</sup> and Kou and Mehrabian<sup>(4)</sup>. Fig. 17 which represents a conduction limited track shows the same kind of form as that predicted by Kou. Kear's one dimensional model predicts a generally much steeper increase in cooling rate up to an equilibrium value. Fig. 16 which represents a keyhole track shows an area where the cooling rate is higher than the material above it this is due to the three dimensional cooling of the thin neck of the keyhole. As would be expected higher cooler rates are obtained with the smaller melt volume of the conduction limited track (an order of magnitude difference).

#### CONCLUSION

This is a preliminary survey of some results from the 3D finite difference models being developed at University of Illinois and Imperial College. These models are being developed to minimise the number of assumptions which need to be made in the theoretical predictions of laser/material processes.

Currently the models are being used to study the effect of latent heat on weld pool characteristics; the correlation of operating parameters with effects within materials, the mapping of important metallurgical parameters (such as G.R and G/R) and analysis of various physical models of the laser/material interaction of latent heat, variable reflectivity, variable thermal properties and keyholing.

#### ACKNOWLEDGEMENTS

Both the groups in the University of Illinois and that at Imperial College would like to thank the USAF for allowing this cooperation to take place.

P. Henry would like to acknowledge the support of IMI (Titanium) Ltd and the Science & Engineering Research Council for a studentship.

T. Chande would like to acknowledge support from American Iron & Steel Inst.

#### REFERENCES

1. Mazumder, J., Steen, W.M., J. App. Phys. 51 (2) Feb. 1982
2. Dean, J.H., Breinan, E.M., Greenwald, L.E., Penas, G.M., ASM Trans. Laser M.I. 78-987 1976.
3. Fealy, J.F. Effects of high power laser radiation. Academic Press 1978 p. 1.
4. Ebu, S., PSU, S.C., Mehrabian, R. Met. Trans. vol. 12B pp. 42-43, March 1981
5. Ebu Ph.D. thesis. London. 1979

#### MEET THE AUTHORS

Paul Henry after obtaining a degree in metallurgy at Imperial College in 1980 is now studying for a doctorate at Imperial College.

Tushe Chande obtained a degree in metallurgy at IIT Kharapur in 1980 and is now studying for a doctorate at the university of Illinois.

Kieth Lipscombe obtained a degree in physics in 1975 and an MSc in material sciences in 1976, doctorate in metallurgy at Imperial College in 1980 and is currently a research assistant at Imperial.

Jyoti Mazumder obtained a degree in metallurgy at Calcutta university in 1973, a doctorate in laser processing at Imperial College 1978 and is currently an assistant professor at the university of Illinois.

Bill Steen obtained a degree in Chemical Engineering at Cambridge University in 1958, a doctorate in laser processing at Imperial College in 1976 and is currently a lecturer at Imperial College, London University.

## APPENDIX B

### ESTIMATING EFFECTS OF PROCESSING CONDITIONS AND VARIABLE PROPERTIES UPON POOL SHAPE, COOLING RATES AND ABSORPTION COEFFICIENT IN LASER WELDING

by

T. Chande and J. Mazumder ,

Materials and Design Division

Department of Mechanical and Industrial Engineering

University of Illinois at Urbana-Champaign

1206 W Green, Urbana, IL 61801

#### ABSTRACT

This paper examines the role of traverse speed, Beer Lambert absorption coefficient,  $\beta$ , surface reflectivity and changing liquid thermal conductivity upon the shape of the melt pool, and the cooling rates that occur. The dependence of  $\beta$  upon processing conditions is also examined. A three-dimensional variable property, moving heat source, quasi steady state, finite difference model for heat conduction into the substrate during laser welding is used. With an increase in traverse speed, the pool flattens out, is swept back, and cooling rates increase. An increase in  $\beta$  sharply decreases the depth of penetration. With the onset of melting, changes in reflectivity did not change pool shape significantly. An increase in effective liquid metal thermal conductivity increases melt pool aspect ratio. Cooling rates increase as



the energy density in the pool decreased. A dimensionless melt front velocity,  $\phi$ , is defined such that cooling rates exceed 1000 K/s as  $\phi$  approaches unity. The product  $\beta z$ , where  $z$  is the depth of penetration, is shown to vary linearly with the natural logarithm of  $\phi$ . These results imply that  $\beta$  affects depth of penetration more than the width, that an upper bound for  $\beta$  may be deduced from  $\phi$ , that variations in surface reflectivity are less critical in laser welding, that the maximum thickness that can be welded in a single pass decreases as fluid flow becomes more dominant in the melt pool, and that cooling rates increase as pool energy density decreases, especially for values of  $\phi < 100$ .

## 2. INTRODUCTION

Laser welding has received much experimental attention[1], but not all the physical phenomena involved are fully understood. Laser material interactions consist of complex, and generally short-lived, but intense events. Many important aspects and effects of these interactions are not directly, or routinely measureable, such as the absorption coefficient in the keyhole, and the temperature and fluid flow velocity distributions. It is also somewhat difficult to isolate the effect of a particular variable without extensive experimentation, due to the many substrate properties, and operating conditions, contributing to the observed effects. On the other hand, a mathematical model, based upon insights gained during experimentation, can be used to calculate the above parameters. A mathematical model, within the limitations of the assumptions made in the formulation, offers a powerful alternative to a purely experimental approach in identifying important process mechanisms and trends, which can be used to obtain better laser welds.

This paper examines the role of traverse speed, surface reflectivity, Beer Lambert coefficient, and changing liquid thermal conductivity, on the shape of the melt pool, and the

cooling rates that occur. Dependence of absorption coefficient on processing conditions is also examined. A modified form of a finite difference, heat conduction model[2], that now allows for temperature dependent substrate properties, in addition to keyholing, and surface convective and radiant heat losses is used for the purpose. A variable property model is a more realistic approximation of the substrate's response to laser irradiation. The model calculations are of interest, as the pool shape determines the magnitude and distribution of cooling rates, as well as the maximum thickness that can be welded in a single pass. Cooling rates, in turn, govern the solidification behaviour, and the nature, extent, and fineness of solid state phase transformations that occur, including the extent of the heat affected zone. Knowledge of the absorption coefficient is desirable, for it determines the laser power required for a desired melt depth.

A review of earlier models for laser welding appears in [2]. A moving line-source model with non-uniform heat input[3], and a model with heat flow in V and U grooves in three-dimensions using variable properties[4] are among those proposed. A model for surface melting with a scanning laser, that obtains the temperature distribution by superposing the known Green's function solution for the thermal distribution for a unit

point source has been reported[5]. Cline and Anthony[5] assume constant substrate properties, no surface heat losses, and do not account for keyholing or heats of transformation. Using an approximate exponential relation for temperature penetration into the substrate, they estimate the depth of penetration for laser welding, and report good agreement for 304 stainless steel for depths greater than 1 cm. A three-dimensional moving heat flux numerical model for rapid melting and solidification of a surface has recently been published[6]. This model provides information on the solidification behaviour of laser melted materials, but its application to laser welding is limited because keyholing, surface heat losses and variable substrate surface and bulk properties have not been considered.

Results of present calculations show that with an increase in speed, the pool flattens out, is swept back, and cooling rates increase near the pool surface and edges. An increase in Beer Lambert coefficient,  $\beta$ , sharply decreases the depth of penetration. With the onset of melting, sensitivity to variations in surface reflectivity is reduced. As the thermal conductivity of the melt pool was increased, for a given set of operating conditions, shallower pools, with a higher aspect ratio were obtained. Cooling rates increased as the energy density in the pool decreased. A dimensionless melt front

velocity,  $\phi$ , is defined, ( see APPENDIX), that provides an upperbound for processing conditions, such that cooling rates exceed 1000 K/s as  $\phi$  approaches unity. An equation to estimate an upperbound for the Beer Lambert absorption coefficient,  $\beta$ , using  $\phi$  is derived. The product  $\beta z$ , where  $z$  is the depth, was found to be linear function of the natural logarithm of  $\phi$ .

### 3. THE MODIFIED MODEL

A moving heat source model for three dimensional heat conduction in the substrate during laser materials processing is used. It calculates temperature fields, melt widths and depths of penetration. A quasi steady-state is assumed to exist, and allowance made for keyholing, laser beam mode structure, variable substrate properties, and surface heat losses from a semi-infinite slab of finite thickness. The major modifications are the incorporation of variable substrate bulk and surface properties, and a change in the method of solution to a point successive overrelaxation scheme. A linear grid is incorporated as an option, and the listing has been streamlined to reduce execution time. For other details, see [2,7].

The assumptions are:

1. The laser beam is stationary relative to the earth, and is incident at right angles at the center of the substrate width. The substrate moves in the positive  $x$  direction, (along the length), with a uniform velocity,  $u$ , and is infinite in length, but has finite width and thickness.

2. Quasi-steady state is assumed.
3. The power distribution in the beam is Gaussian.
4. The substrate thermal conductivity, specific heat, thermal diffusivity and the surface reflectivity are temperature dependent. The substrate density is assumed to be independent of temperature. Specific heat variation accounts for heats of fusion and vaporization by converting them into equivalent step increases in values of specific heat, as for example,

$$\bar{C}_p \Delta T_m = \int_{T_o}^{T_m} C_p dT + L \quad 1$$

5. Surface reflectivity is considered to be zero when the temperature exceeds the boiling point.
6. There is a radiation loss at the upper and lower surfaces of the workpiece.
7. Convective losses occur at the upper surface due to shielding gas flow.
8. When the temperature at any location exceeds the boiling point, it is considered to have evaporated, but remains in the conducting network at a fictitiously high temperature, to simulate the effect

of high convection and radiation transfer effects from the fast moving plasma in the keyhole.

9. Radiation penetrating the substrate is absorbed according to the Beer-Lambert law,

$$P_z = P_s \exp(-\beta z) \quad 2$$

where  $\beta$  is the absorption coefficient ( $m^{-1}$ ) and is considered independent of position within the keyhole, and  $P_z$  is the absorbed power density at depth  $z$  which was of value  $P_s$  at the surface.



#### 4. MODEL CALCULATIONS

Calculations were made for a Ti-6AL-4V substrate. Data on property variation (Fig. 1-3) in the solid state are from published literature[8]; projections above melting point are thought to be reasonable approximations of the expected behaviour. Actual data for these high temperatures are unavailable.

Changes in pool shape and variations in cooling rates were the two areas of interest. Changes in depth of penetration, and in surface melt widths were used to quantify variations in pool shape. Computer calculations were made to find the effects of changes in traverse speed, Beer Lambert coefficient,  $\beta$ , effective thermal conductivity in the liquid state, and surface reflectivity upon pool shape. Overall rates of heat transfer are increased by convective heat transport, due to fluid flow in the melt pool. This effect is approximated by arbitrarily increasing the effective thermal conductivity in the liquid state in the model as it assumes a static pool. Temperature gradients in the x-direction, and the traverse speed, were used to determine the variations in cooling rate with melt depth and traverse speed. The cooling rates were related to the energy density in the pool, assuming

good coupling between the laser and substrate. A dimensionless melt front velocity,  $\Phi$ , was defined, where

$$\Phi = (P/d^2)/(u\rho\bar{C}_p\Delta T_m) \quad 3$$

Using  $\Phi$ , it is possible to compute an upper limit to the value of the absorption coefficient, (see APPENDIX), and effective limiting values for different energy densities in the pool are calculated. The value of the depth of penetration used to calculate  $\Phi$  here, are derived from the model itself, for a constant  $\beta$  value of 1000.

It should be noted, that  $P/ud^2$  is only a measure of the actual energy density in the melt pool, as it assumes that the melt pool is a rectangular parallelepiped, of crosssection  $d^2$ , of length  $u$ , which absorbs  $W$  joules of energy every second. It assumes that no losses occur into the substrate, and that laser-substrate coupling is perfect. In practice, under steady state conditions, the actual energy density will be a constant fraction of this estimate (see also [9]).

## 5. MODEL RESULTS

With an increase in speed, the the pool flattens out, is swept back, and the leading edge makes a smaller angle with the center line (Fig. 4-6). The point of highest temperature shifts behind the laser beam. The width decreases too, but not as sharply as the depth. For a given incident power density, an increase in speed, increases cooling rates, with higher rates being observed near the surface and the edges of the melt pool (Fig. 7,8). An increase in  $\beta$  results in sharp decrease in depth (Fig. 9), while the width of the pool is not affected as much. If the surface reflectivity is too high, (0.99 say), no melting occurs (Fig. 10). However, if the reflectivity is such that the fraction of energy absorbed is sufficient to initiate melting, then, the sensitivity to changes in reflectivity is greatly reduced.

Increased effective thermal conductivity in the liquid state can significantly affect the shape of the weld puddle (Fig. 11). The aspect ratio of the pool increases as the Peclet number ( $ud/\alpha$ ) decreases. The decrease in depth implies that materials with a higher thermal conductivity are harder to weld, as is observed in practice, for a given set of operating conditions.

As the energy density ( $\text{J/mm}^3$ ) of the pool decreases, cooling rates increase (Fig. 12). Cooling rates in excess of ten thousand degrees a second are obtained when values of the dimensionless melt front velocity are less than a hundred (Fig. 13). Changes in energy density in the pool also affect the values of the Beer Lambert absorption coefficient,  $\beta$ , with the product of  $\beta$  and  $z$ , the depth of penetration, being linearly related to the natural logarithm of  $\phi$ , the dimensionless energy density, (Fig. 14).

## 6. DISCUSSION

The paucity of high temperature material property data is a source of major difficulty in using variable property models. An assumption of constant properties is unrealistic, and leads to predictions of doubtful value. In the present model, the variation in thermal conductivity at high temperature reflects the expected effects of convective heat transport due to fluid flow in the melt pool, and the rapid heat transfer in the plasma filled keyhole. Specific heat variation accounts for heats of fusion and vaporization. The heats of transformation are easily converted to specific heat equivalents. The thermal diffusivity is derived from the conductivity and specific heat, assuming a constant substrate density. While the arbitrary choice of these temperature dependencies is unavoidable, the assumed temperature dependence is crucial to model results. Hence, it is the trend that emerges, rather than the exact numerical value, which is of greater importance here.

As the traverse speed increases, the time of interaction between the laser and the substrate decreases. This results in shallower, colder pools, as the substrate absorbs a smaller amount of the incident energy. Also, front-to-back velocity

of the molten material increases, so that convective heat transport past the beam increases, resulting in pools that are swept back. Both these factors lead to Fig. 4-6. The shallower, colder pools have a higher surface area per unit volume, in contact with a relatively cooler substrate. They are thus subjected to higher rates of heat extraction by the substrate, and cooling rates increase. In general, cooling rates increase as solidification proceeds towards the surface[10], as happens at the trailing edge of the pool. While this information is not entirely new(see [5],[11]), it does serve as a check on model predictions.

Laser radiation couples to a substrate better when it is molten rather than solid[12]. Thus, small variations in solid reflectivity will have a lesser effect if the laser is incident upon a pool of molten material at the surface (Fig. 10). Surface reflectivity variations will be more critical during laser heat treatment, when no surface melting occurs, than during laser welding or alloying.

Since this model does not explicitly allow for fluid flow, the increased convective heat transport away from the beam can only be accounted for in an approximate way, by increasing the effective liquid thermal conductivity(Fig. 11). The trend

there is reasonable, in that the aspect ratio increases as fluid flow becomes more vigorous, or effective thermal conductivity increases. Actually, flow at the surface will increase melt widths, and reduce depths, as more material is melted by heat transported laterally away from the beam. It also implies, that if an arbitrary increase in effective liquid conductivity is assumed in models with constant substrate properties[6], then the choice largely dictates the predicted melt pool shapes.

A measure of the rate at which the solid-liquid (S-L) interface sweeps through the material is provided by the cooling rate. In laser welding, solidification occurs at the S-L interface trailing the beam, and moving with it. The cooling rate, except for starting and stopping transients, is determined by the rate at which this part of the S-L interface travels through the substrate. As  $\phi$  approaches 1, the S-L interface will sweep through the material at faster velocities, increasing cooling rates. Hence,  $\phi$  may be used to estimate a working range of processing conditions, where we can expect high cooling rates (Fig. 13).

$\phi$  is also the ratio of the energy density in the pool to that required to cause melting. As  $\phi$  approaches 1, the

superheat in the pool, decreases, so that the pool will be subjected to higher rates of heat extraction, increasing cooling rates (Fig. 12).

In modeling of laser processes, as well as in practice, a knowledge of the absorption coefficient,  $\beta$ , is desirable. In as much as  $\beta$  has not been directly measured, the equation for estimating an upperbound on  $\beta$  should be quite useful. A better estimate can be obtained, if actual depths of penetration are used, with the energy density required to initiate melting. Both these quantities are readily measured experimentally.  $\beta$  can be estimated if the depth of penetration is known, and the constant A is estimated from experiments, by using the relationship plotted in Fig. 14.

The results of this model are relevant to laser welding. The effects of a change in the absorption coefficient, its variation with pool energy density provide new insights. A means to estimate an upperbound for  $\beta$  is useful. The role of varying reflectivity, and increased fluid thermal conductivity in the pool point to important mechanisms. A knowledge of the variation of cooling rates with energy density, and a means of selecting operating conditions that will produce high cooling rates via  $\phi$  should help in the production of better welds.



## 7. CONCLUSIONS

The following conclusions can be drawn from the above results:

1. The absorption of laser energy in the keyhole, as determined by the Beer Lambert coefficient  $\mu$ , affects the depth of penetration more than the width of the weld.
2. Variations in the surface reflectivity are less critical in laser welding or alloying, as surface melting occurs.
3. The aspect ratio of the weld pool increases, as effective liquid thermal conductivity increases, with an increase in the vigor of fluid flow in the melt pool.
4. Cooling rates increase as the energy density in the melt pool decreases.
5. An operating region of high cooling rates may be estimated using the dimensionless melt front velocity,  $\phi < 100$ , where

$$\phi = (P/d^2) / (u_p \bar{C}_p \Delta T_m)$$

4

6. An upperbound for  $\beta$  may be estimated, using

$$\beta = \frac{1}{z} \ln (A \dot{\epsilon}) \quad 5$$

where the constant A can be determined from the experimentally determined power density required to initiate melting at that speed as

#### ACKNOWLEDGEMENT

This work has been supported by European office of Air Force Research and Development. This is a joint program with Imperial College of Science and Technology, London, United Kingdom.

## 8. REFERENCES

1. J. Mazumder, J. Metals, 34(7), 16, (1982).
2. J. Mazumder and W. M. Steen, J. Appl. Phys., 51(2), 941, (1980).
3. Y. Arata and K. Inoue, Trans. JWRI, 2(1), 41, (1973).
4. Z. Paley and P. D. Hibbert, Welding J., 54, 385S, (1975).
5. H. E. Cline and T. R. Anthony, J. Appl. Phys., 48(9), 3895, (1977).
6. S. Kou, S. C. Hsu and R. Mehrabian, Metall. Trans., 12B(1), 33, (1981).
7. T. Chande and J. Mazumder, "Lasers in Metallurgy", K. Mukherjee and J. Mazumder, eds., 165, AIME, (1981).
8. "Thermophysical Properties of High Temperature Solid Materials", Y. S. Touloukian, ed., MacMillan Co., New York, (1967)  
See also, "Thermophysical Properties of Matter", Y. S. Touloukian, C. S. Ho, eds., Vols. 1, 4, 7, 10, IFI/Plenum, New York, 1970.
9. C. Courtney and W. M. Steen, Paper 2, "Adv. in Surface Coating Tech. Int. Conf.", Welding Inst., UK, 219, (1978).
10. T. Chande and J. Mazumder, Metall. Trans., 14B(2), 181, (1983).
11. J. A. Sekhar, S. Kou and R. Mehrabian, Metall. Trans., 14A(6), 1169, (1983).
12. S. L. Engel, Laser Focus, 12(2), 44, (1976).

## 9. APPENDIX

A simple one-dimensional model may be used to relate the incident energy flux,  $P/d$  to the sweep rate of the solid-liquid interface, and the cooling rates. For a thin layer of molten material at the surface, a heat balance indicates that to melt an incremental amount of material

$$\frac{P}{d^2} - k_s \frac{dT}{dz} = \rho \bar{C}_p \Delta T_m \frac{dz}{dt} \quad A-1$$

where, the left hand side represents the incident heat flux, corrected for heat loss into the substrate by conduction. The right hand side is the incremental rate of enthalpy change. The limiting rate of melting is achieved when the heating is so rapid, that very little heat is lost by conduction into the substrate. The limiting melt front velocity would then approach

$$\frac{dz}{dt} \rightarrow (P/d^2) / (\rho \bar{C}_p \Delta T_m) \quad A-2$$

If this is scaled by the traverse speed, the dimensionless upper bound on the melt front velocity is obtained, and

$$\phi = (P/d^2) / (u_p \bar{C}_p \Delta T_m) \quad A-3$$

Assuming that a cylindrical keyhole exists in the melt pool, at the bottom of which, the laser is actually incident on a

portion of the substrate itself, melting will occur only if the irradiation intensity is greater than the energy density required to produce melting. The energy density at the bottom of the pool is  $AP_z/u$ , where  $A$  is a constant,  $u$  is the traverse speed, m/s, and  $P_s$  is the power density,  $W/m^2$ . For melting to occur,  $AP_z/u$  must at least equal  $\rho \bar{C}_p \Delta T_m$ . Using the Beer Lambert law, and substituting for  $P_z$ , we obtain

$$\frac{u \rho \bar{C}_p \Delta T_m}{A} = P_s \exp(-\beta z) \quad A-4$$

Recognizing that  $P_s / u \rho \bar{C}_p \Delta T_m$  is just the dimensionless melt front velocity,  $\phi$ , we obtain

$$\beta z = \ln(A \phi) \quad A-5$$

The constant  $A$  may be estimated if the power density to initiate melting,  $(P/d^2)_{\text{expt}}$  at that speed is determined experimentally. Then,

$$A = (u \rho \bar{C}_p \Delta T_m) / (P/d^2)_{\text{expt}} \quad A-6$$

In the keyhole, the reflectivity is assumed to be zero, due to internal reflections. In actual practice, there will be a layer of liquid between the bottom of the keyhole and the unmelted substrate. Thus, excess heat energy, will have to be supplied at the bottom of the keyhole, to heat fresh substrate through the liquid layer at the floor of the keyhole. Hence, this estimate of  $\beta$  is an upperbound.

## 10. LIST OF CAPTIONS

1. Variation with temperature of thermal conductivity for Ti-6Al-4V. Data above melting point are arbitrary.
2. Variation with temperature of specific heat for Ti-6Al-4V. Data above melting are arbitrary, and have been adjusted for heats of melting and vaporization.
3. Variation with temperature of thermal diffusivity for Ti-6Al-4V, derived from Fig. 1 and 2, assuming constant substrate density.
4. Predicted melt pools, assuming Beer Lambert coefficient of  $1000 \text{ m}^{-1}$ .
5. Predicted melt pools, assuming Beer Lambert coefficient of  $1000 \text{ m}^{-1}$ .
6. Predicted melt pools, assuming Beer Lambert coefficient of  $1000 \text{ m}^{-1}$ .
7. Center line cooling rate at the surface, for laser power of 2kW, and beam diameter of 0.2 mm. Note how

point of peak temperature shifts with increasing speed. Cooling rates plotted for trailing half of pool. Abcissa shows distance behind beam center.

8. Center line cooling rate 0.4 mm below surface, for laser power of 2kW, and beam diameter of 0.2 mm. Note how point of peak temperature shifts with increasing speed. Cooling rates plotted for trailing half of pool. Abcissa shows distance behind beam center.
9. Predicted melt fronts for different values of Beer Lambert coefficient.
10. Predicted melt fronts for different values of surface reflectivity. Note that for reflectivity of 0.99, model predicts no melting will occur. Assumed of Beer Lambert coefficient  $1000 \text{ m}^{-1}$ .
11. Predicted melt fronts for different values of effective thermal conductivity.
12. Variation of center line cooling rate near beam, with estimated melt pool energy density.
13. Variation of center line cooling rate near beam, with

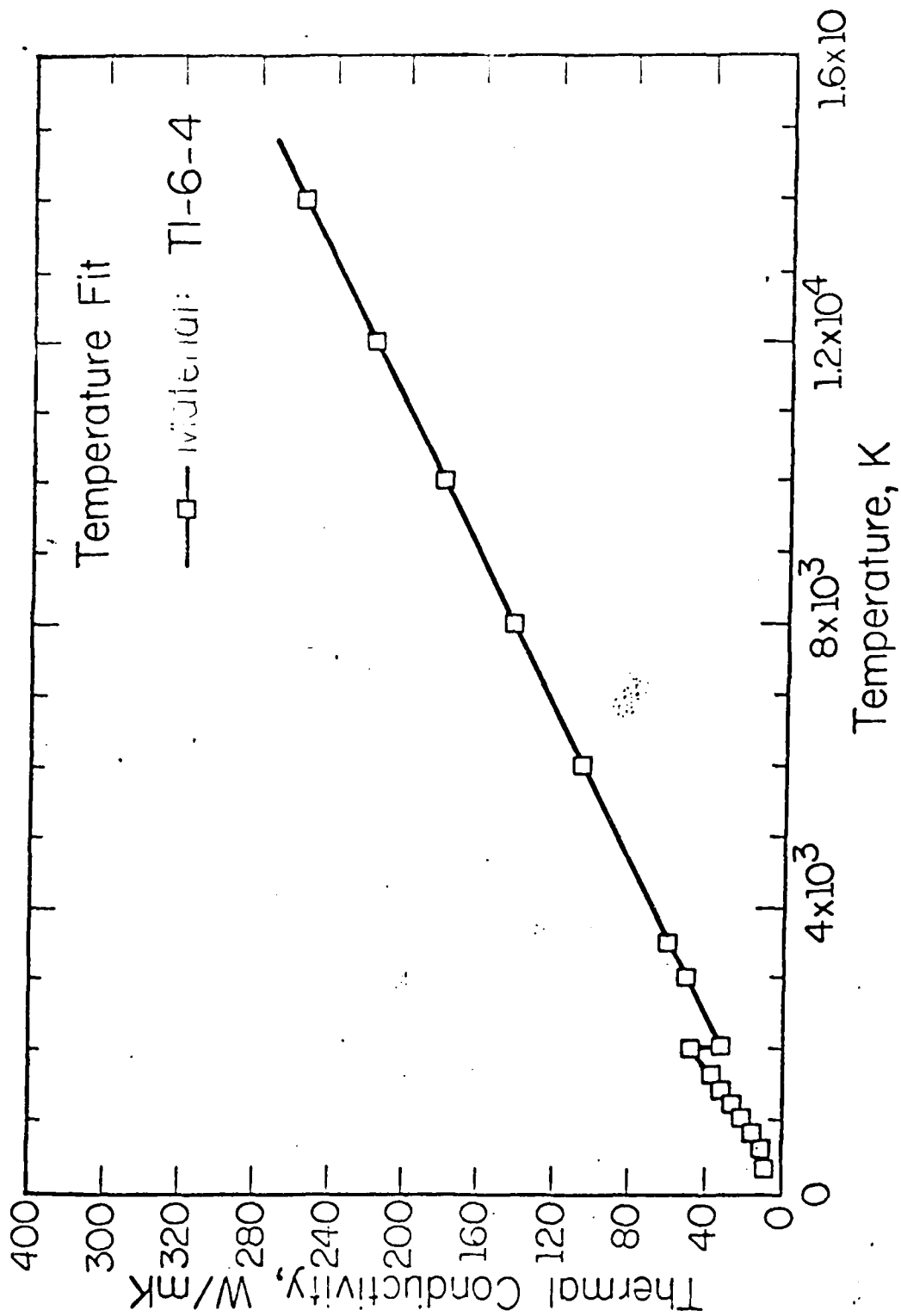
dimensionless melt front velocity.

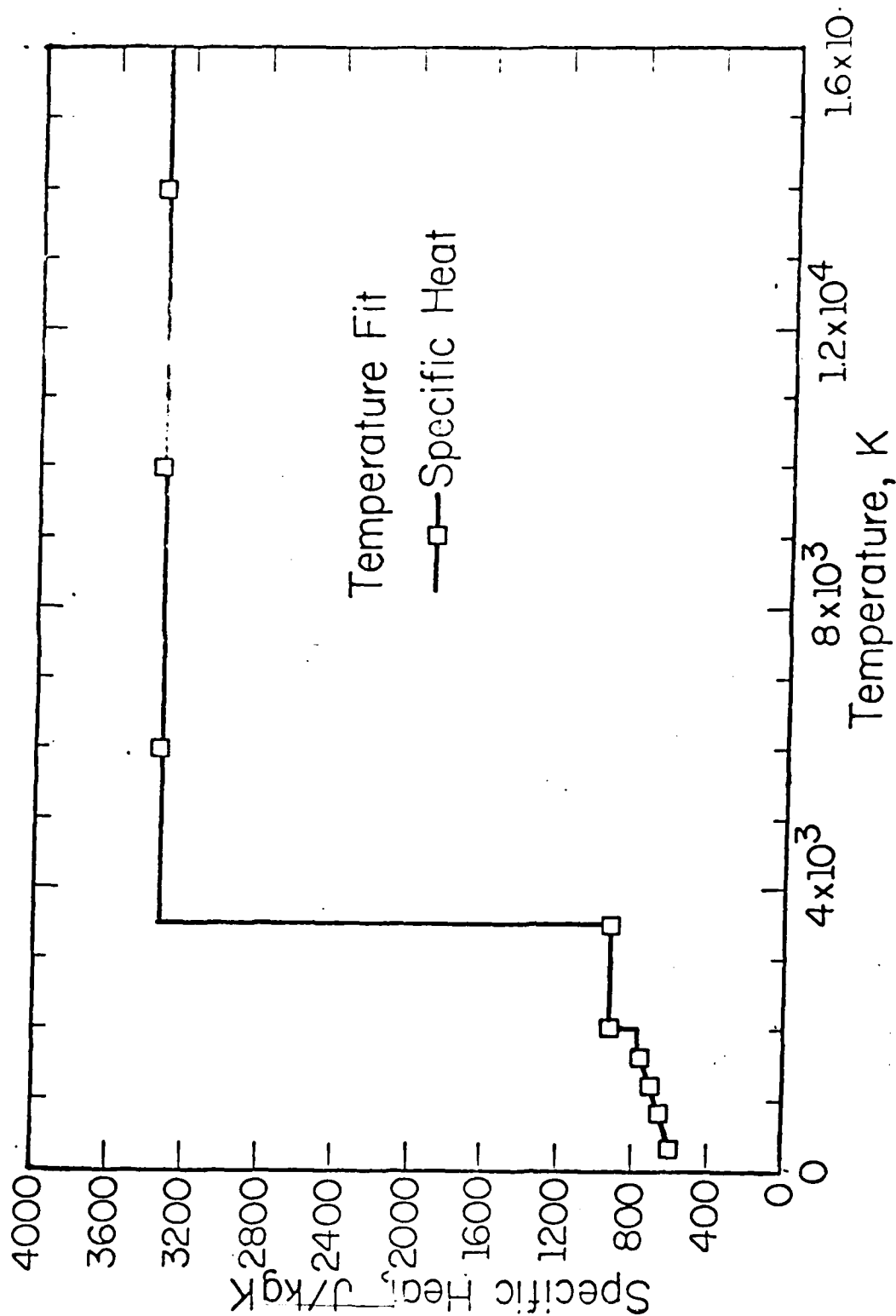
14. Variation in product of Beer Lambert coefficient,  $\hat{\rho}$ ,  $\text{m}^{-1}$ , and  $z$  the depth of penetration,  $\text{m}$ , with changes in dimensionless energy density,  $\Phi$ , for different values of  $A$ .



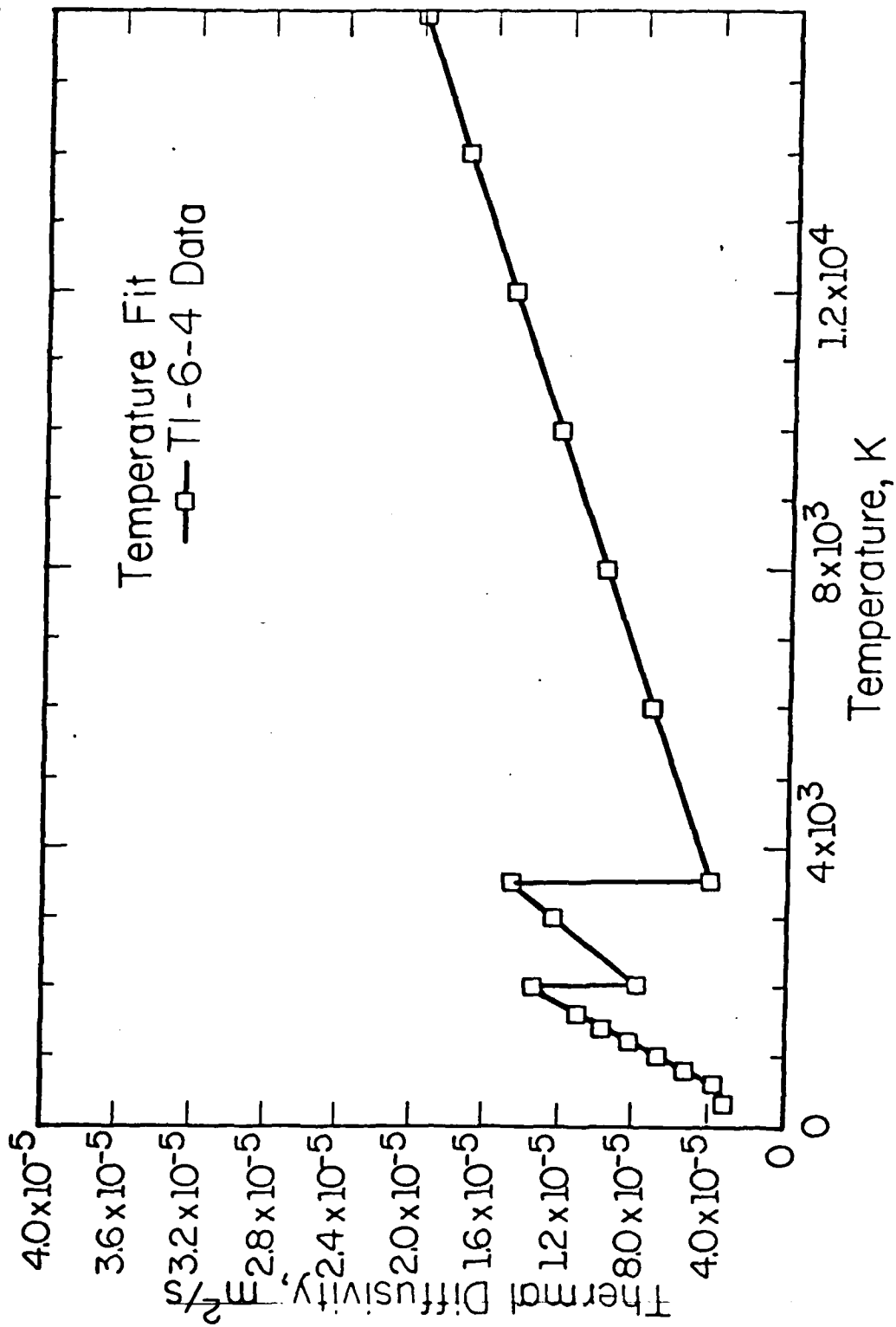
## 11. LIST OF SYMBOLS

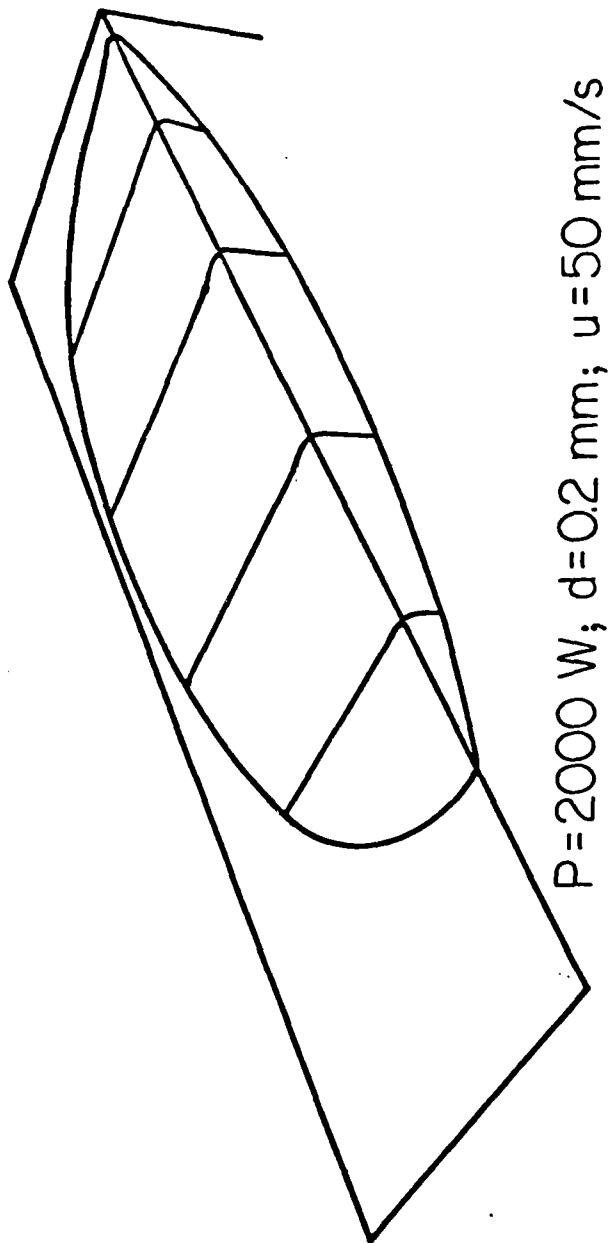
$A$	Constant relating measured and calculated energy density of melting	no unit
$C_p$	Specific heat of substrate	J/kg K
$\bar{C}_p$	Specific heat of substrate corrected for heat of fusion	J/kg K
$d$	Beam diameter	m
$k$	Thermal conductivity of substrate	W/m K
$L$	Latent heat of fusion of substrate	J/kg
$P$	Incident laser power	W
$P_s$	Incident energy flux at surface	W/m <sup>2</sup>
$P_z$	Absorbed power density at depth $z$	W/m <sup>2</sup>
$T$	Temperature	K
$T_o$	Ambient temperature	K
$T_m$	Melting point	K
$\Delta T$	$(T_m - T_o)$	K
$u$	Traverse speed	m/s
$z$	Melt depth	m
$\alpha$	Thermal diffusivity of substrate	m <sup>2</sup> /s
$\beta$	Beer Lambert absorption coefficient	m <sup>-1</sup>
$\rho$	Substrate density	kg/m <sup>3</sup>
$\phi$	Melt front velocity or pool energy density	no unit



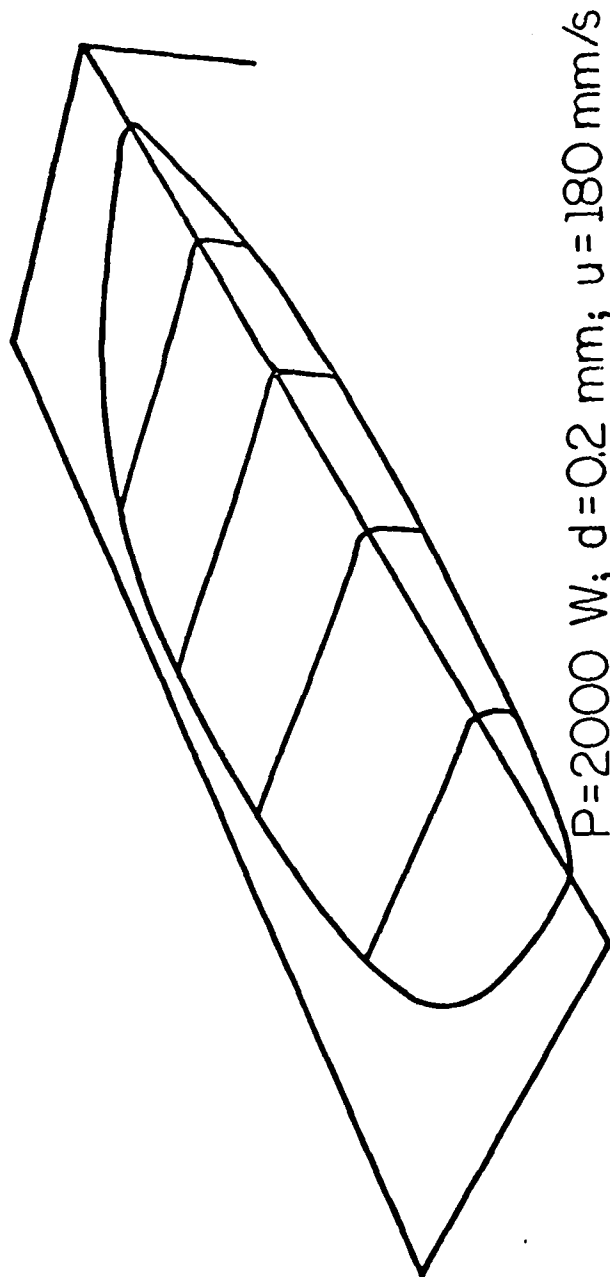


2. Variation with temperature of specific heat for Ti-6Al-4V. Data above melting are arbitrary, and have been adjusted for heats of melting and vaporization.



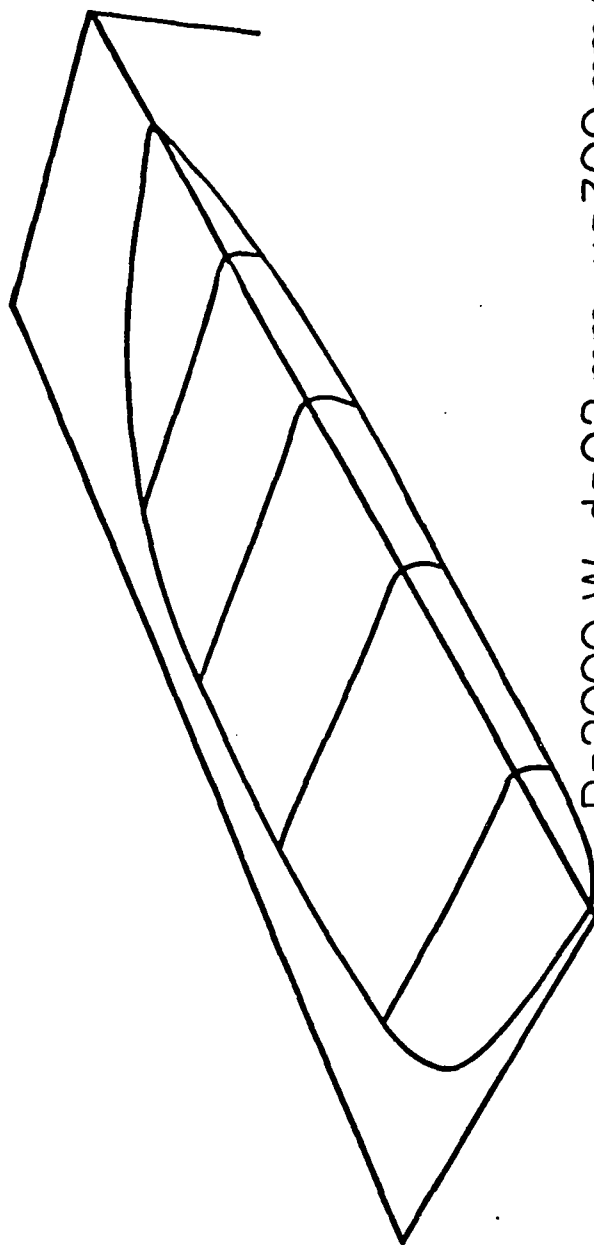


4. Predicted melt pools, assuming Beer Lambert coefficient of  $1000 \text{ m}^{-1}$ .



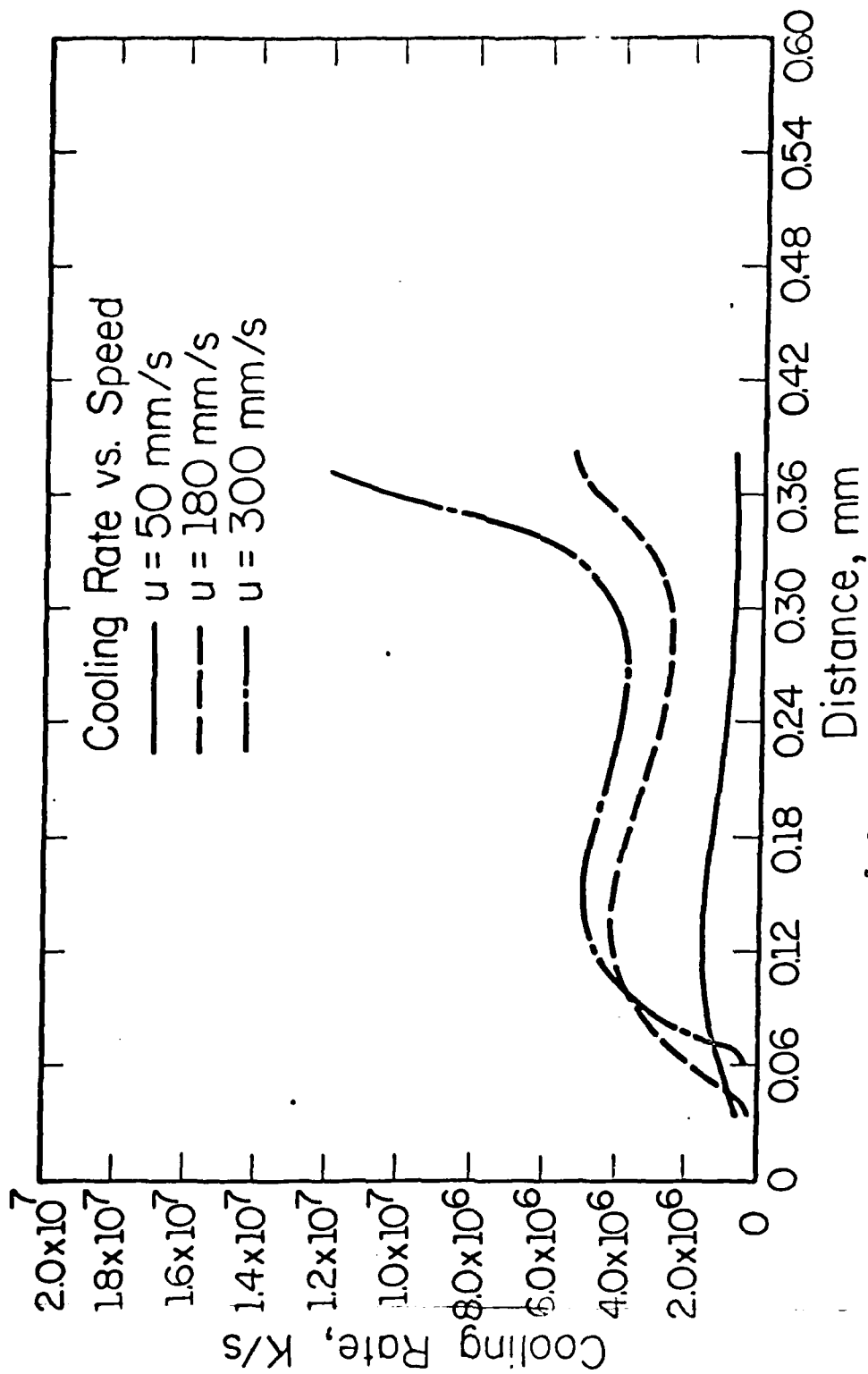
$P=2000 \text{ W}$ ;  $d=0.2 \text{ mm}$ ;  $u=180 \text{ mm/s}$

5. Predicted melt pools, assuming Beer Lambert coefficient of  $1000 \text{ m}^{-1}$ .



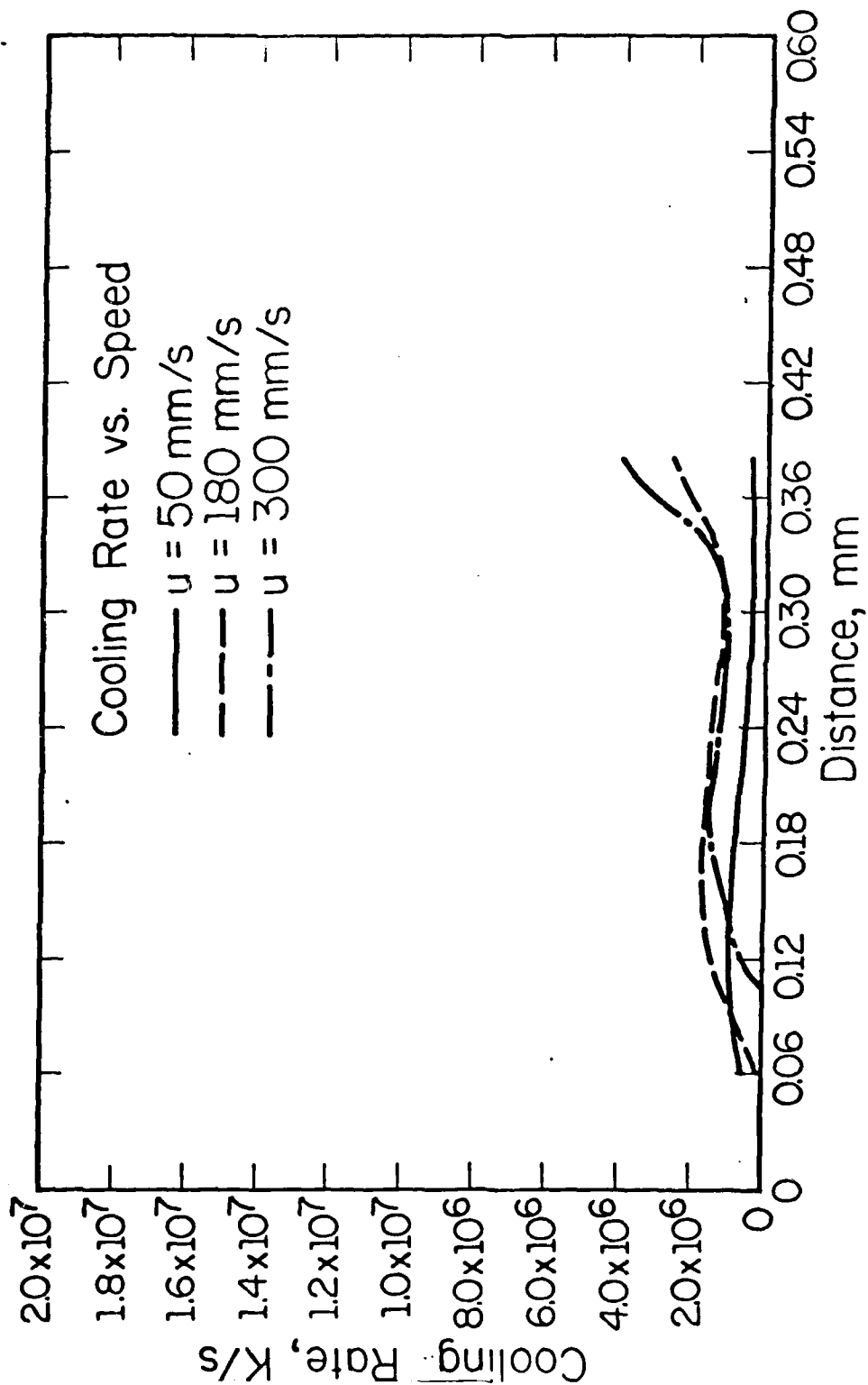
$P=2000 \text{ W}$ ;  $d=0.2 \text{ mm}$ ;  $u=300 \text{ mm/s}$

6. Predicted melt pools, assuming Beer Lambert coefficient of  $1000 \text{ m}^{-1}$ .

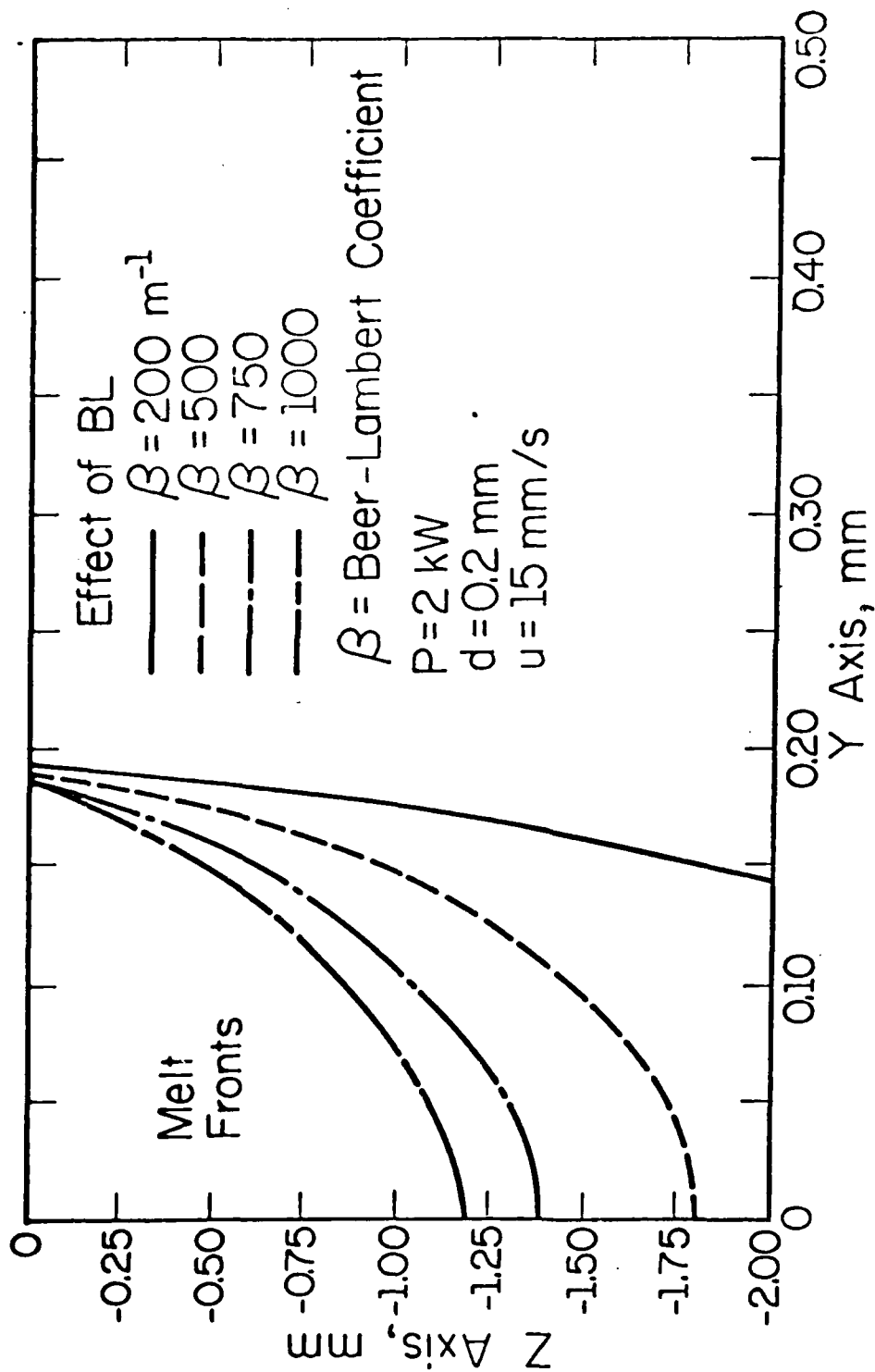


7. Center line cooling rate at the surface, for laser power of 2kW, and beam diameter of 0.2 mm. Note how point of peak temperature shifts with increasing speed. Cooling rates plotted for trailing half of pool. Abscissa shows distance behind beam center.

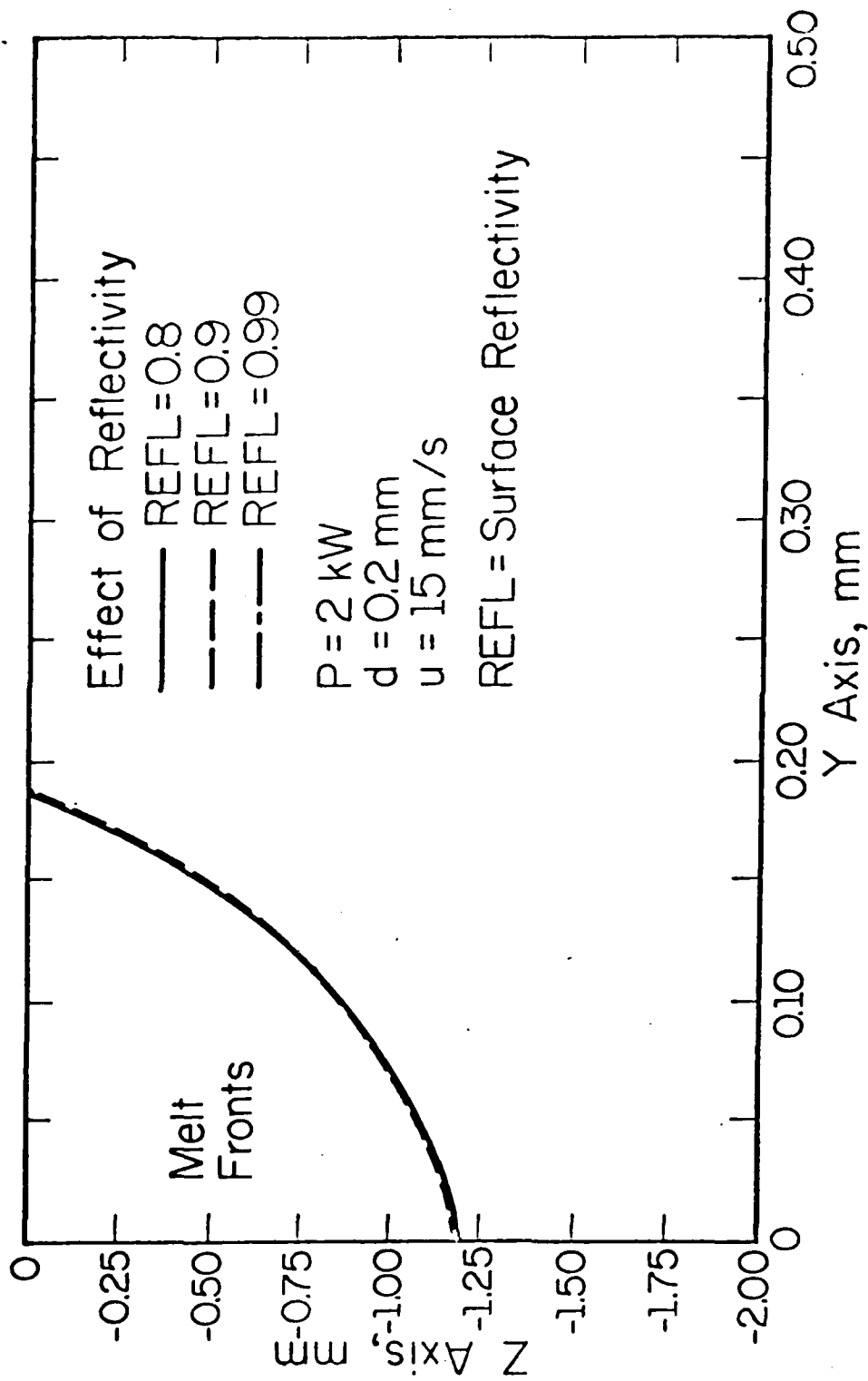




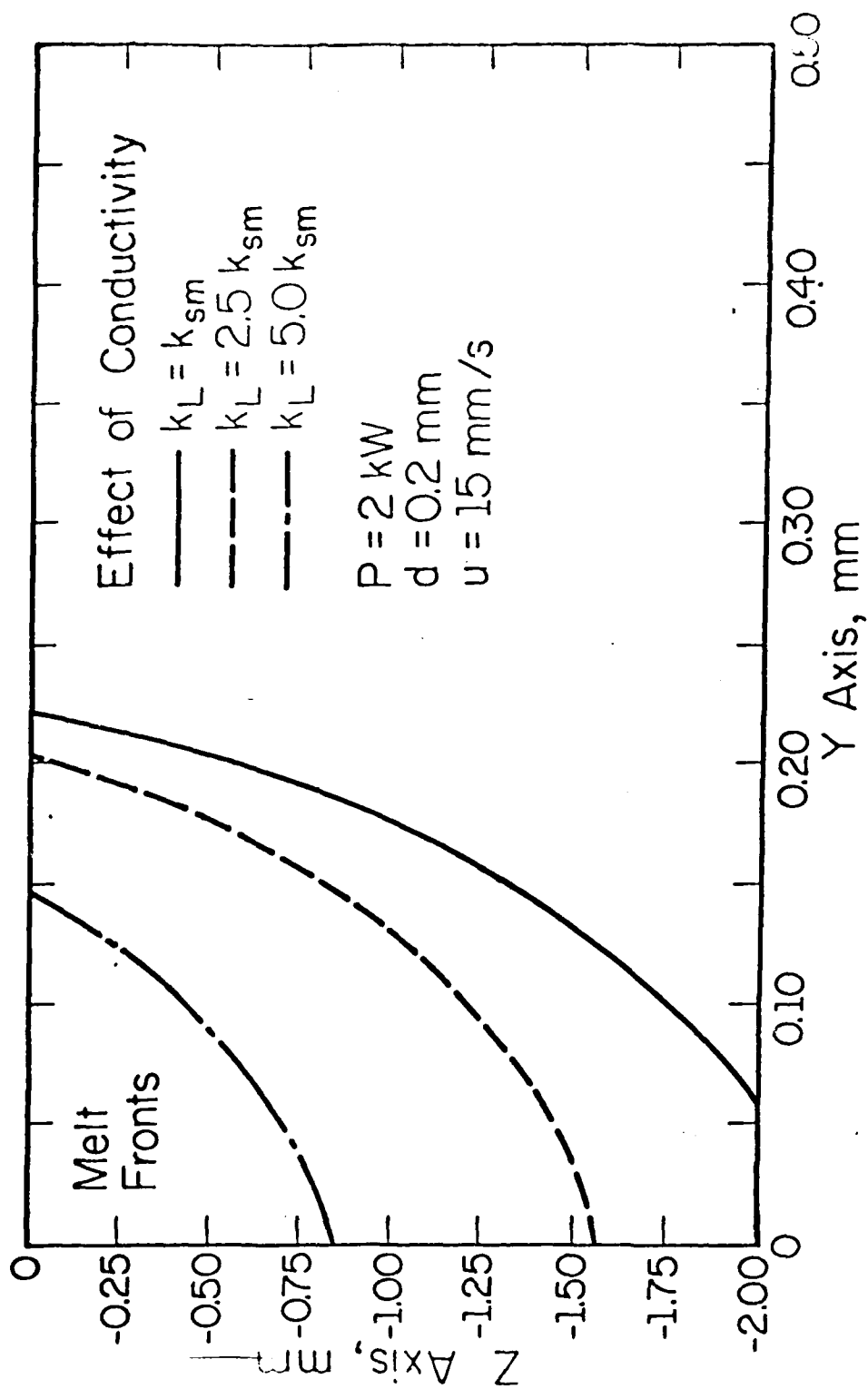
6. Center line cooling rate 0.4 mm below surface, for increasing speed. Cooling rates plotted for trailing laser power of 2kW, and beam diameter of 0.2 mm. half of pool. Abscissa shows distance behind beam center. Note how point of peak temperature shifts with



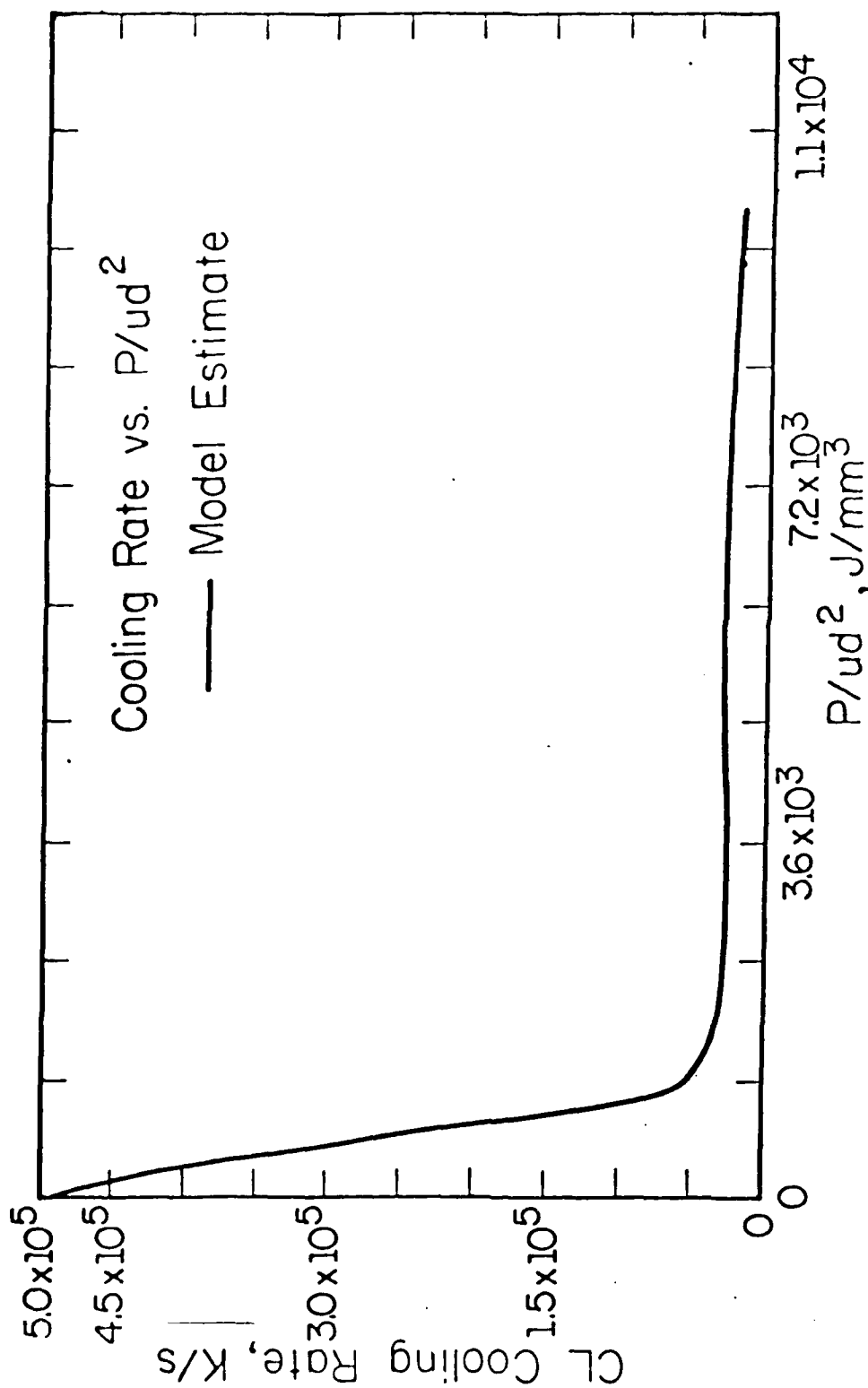
9. Predicted melt fronts for different values of Beer Lambert coefficient.



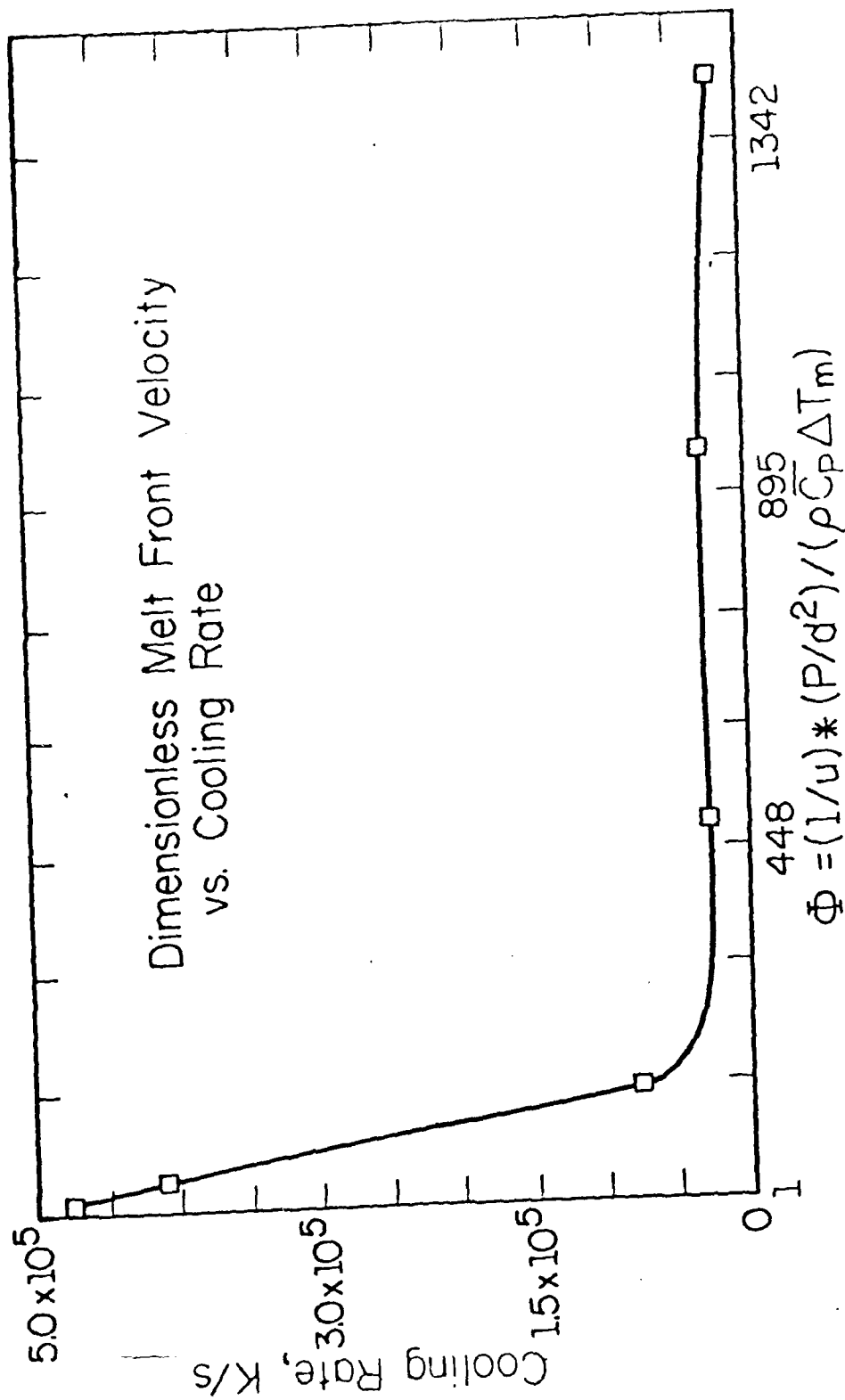
10. Predicted melt fronts for different values of surface reflectivity. Note that for reflectivity of 0.99, model predicts no melting will occur. Assumed of Beer Lambert coefficient  $1000 \text{ m}^{-1}$ .



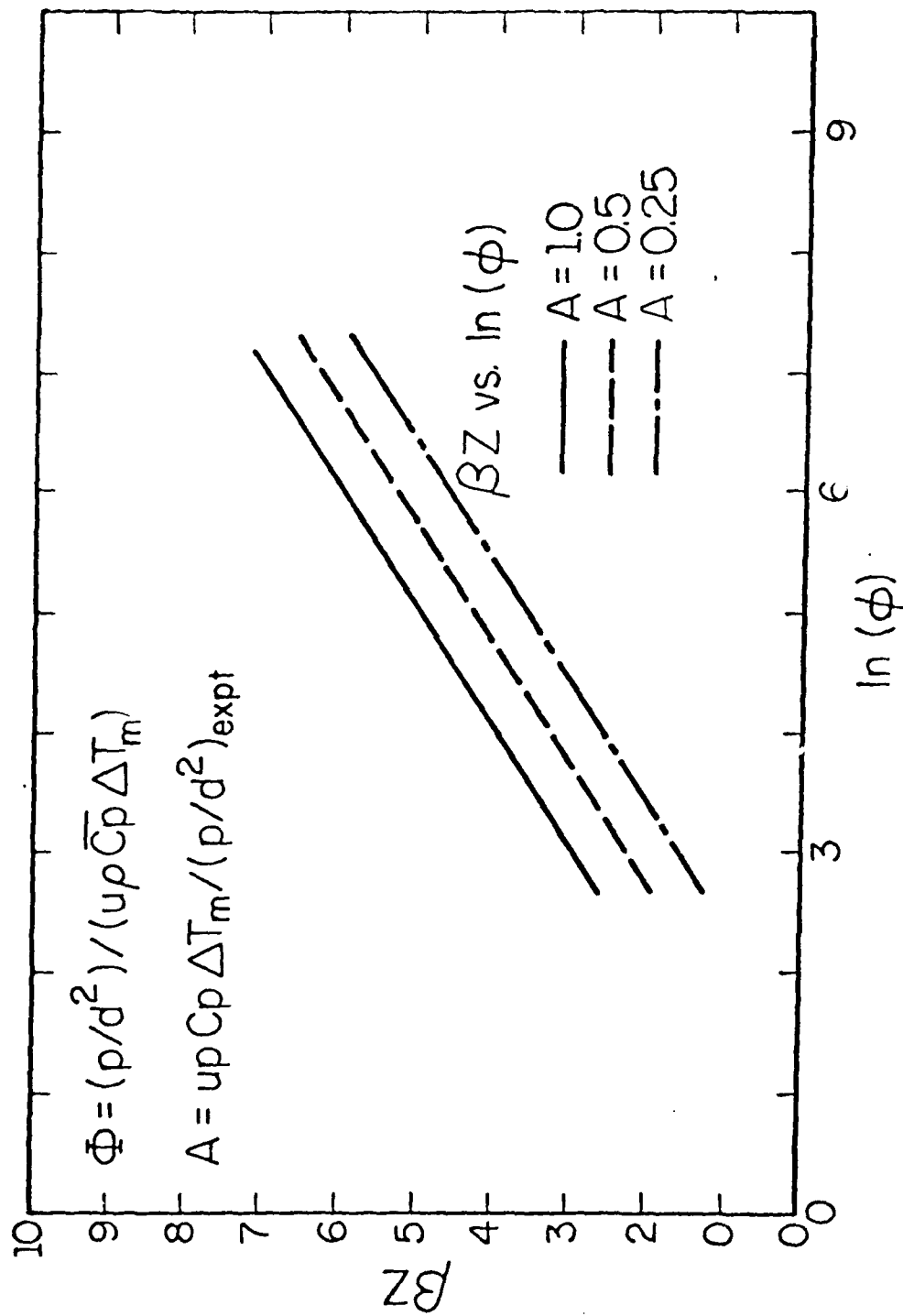
11. Predicted melt fronts for different values of effective thermal conductivity.



12. Variation of center line cooling rate near beam, with estimated melt pool energy density.



13. Variation of center line cooling rate near beam, with dimensionless melt front velocity.



14. Variation in product of Beer Lambert coefficient,  $\beta$ ,  $m^{-1}$ , and  $z$  the depth of penetration,  $m$ , with changes in dimensionless energy density,  $\phi$ , for different

## APPENDIX C

ALAN J. C. SMITH, PH.D., F.R.S., F.R.I., F.R.A.S.  
Imperial College, London, England

M. Sharp, W.M. Steen, P. Henry, G.C. Lim

Imperial College, London, England.

### INTRODUCTION

High power laser welding is now an accepted material processing technique. In gaining this acceptance a large amount of research has been done on the effect of various parameters e.g. traverse speed, laser power, etc. /1,2/. One area which has received little attention is the effect of mode structure of the laser beam on the weld profile.

There are two main reasons why such an investigation is important. First, many of the larger power machines do not produce a Gaussian beam, and so the significance of a non-Gaussian beam is important in assessing the use of these machines. Secondly, since the mode structure of the output from a machine may vary over a period of time, it is necessary to have a knowledge of the effects of the mode structure so that the reproducibility of the weld can be guaranteed.

As a starting point of this investigation, the profile of a focussed beam operating in a TEM<sub>mn</sub> mode is shown to have the same profile as the unfocussed beam when aperture effects are neglected and perfect optics are assumed. From this it can be deduced that the focussed beam has the same intensity as the raw beam for any intensity profile.

A new definition of the spot size is introduced which allows a consistent comparison of the spot sizes of the different modes. Using a finite difference numerical model of the laser welding process an investigation is made into whether the effect of the mode structure on the weld profile is due solely to the varying effective spot sizes of the modes, or whether the actual mode structure itself has an effect.

A theoretical investigation is made into the effect of a finite lens aperture on the spot size, and it is also shown how lens aberrations can be taken into account. Finally an experiment is described to validate the theoretical results outlined in this paper.

### FOCUSING OF LASER BEAMS

The TEM<sub>mn</sub> modes for a laser with cylindrical symmetry are given in /3/ as

$$A_{mn}\left(\frac{r}{w}, \theta\right) = \left(\frac{\sqrt{2}r}{w}\right)^n L_m^n\left(\frac{2r^2}{w^2}\right) e^{-\frac{r^2}{w^2}} e^{in\theta} \quad (1)$$

where  $(r, \theta)$  are polar coordinates,  $w$  is the characteristic radius of the beam.  $L$  is the Laguerre polynomial of order  $n$  and degree  $m$ , and  $A_{mn}$  is the amplitude of the TEM<sub>mn</sub> mode. The intensity is given by

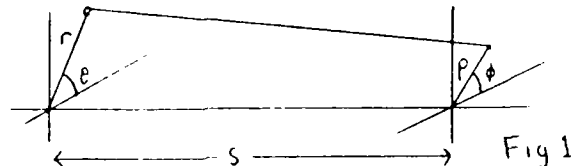
$$I(r, \theta) = |A_{mn}|^2$$

Standard texts on optics (4) derive the following equation for the intensity of a beam of light of wavelength  $\lambda$  passing through a lens of focal length  $f$  and aperture  $D$  at a distance  $z$  from the lens:



$$Q_{mn}(\rho, \phi) = \int_{r=0}^a \int_{\theta=0}^{2\pi} H_{mn}\left(\frac{r}{w}, \theta\right) e^{-\frac{ikr^2}{2f}} e^{\frac{ik}{2}\left(\frac{r^2}{2} - \rho^2 \cos(\theta - \phi)\right)} r dr d\theta$$

where the geometry involved is illustrated in Fig. 1.  $k=2\pi/\lambda$ ,  $f$  is the focal length of the lens, and  $a$  is the aperture radius.



Performing the integration over  $\theta$  yields

$$Q_{mn}(\rho, \phi) = e^{i\pi/4} \int_{r=0}^a A_{mn}\left(\frac{r}{w}\right) e^{-\frac{ikr^2}{2}\left(\frac{1}{s} - \frac{1}{f}\right)} J_n(zr) r dr \quad (4)$$

where  $z=k\rho/s$ . At focus the complex exponential term disappears. Aperture effects can be neglected by taking  $a$  as infinite. In this case it can be shown that

$$Q_{mn}(\rho, \phi) = A_{mn}\left(\frac{\rho}{w_f}, \phi\right) \quad (5)$$

where

$$w_f = \frac{\lambda f}{\pi w}$$

is the characteristic radius of the focussed beam. Since the  $A_{mn}$  form an orthogonal set of functions and (3) defines a linear integral operator on the functions  $A_{mn}$ , then it can be shown that

$$Q(\rho, \phi) = A\left(\frac{\rho}{w_f}, \phi\right) \quad (6)$$

for all beams with unfocussed amplitude  $A(r, \theta)$ .

### SPOT SIZE

There have been many definitions introduced to describe the spot size of the laser beam. The characteristic radius,  $w$ , is not a good measure of the spot size since the effective spot size of the higher order modes is much greater than the characteristic radius. The important point about the characteristic radius is that it is a function of the geometry of the laser cavity alone [3], and is therefore independent of the mode structure.

The one drawback with the characteristic radius and other definitions is that the power contained within the defined radius is dependent on the mode itself.

To rectify this the following definition of spot size is introduced. A laser beam of total power  $P$  and intensity distribution  $I(r, \theta)$  has radius,  $R$ , defined by

$$\int_{r=0}^R \int_{\theta=0}^{2\pi} I(r, \theta) r dr d\theta = (1 - e^{-2})P \quad (7)$$

The factor  $(1 - e^{-2})$  is chosen so that the beam radius  $R$  is equal to the characteristic radius  $w$  for the Gaussian mode. In order to describe the relative sizes of the different modes, a mode factor,  $K$ , is defined by

$$R = Kw$$

Mode factors for the lower order modes are given in table 1 below

TABLE 1  
Mode factors of TEM<sub>mn</sub> modes

		N		
		0	1	2
M	0	1.00	1.32	1.56
	1	1.65	1.88	2.08
	2	2.12	2.31	2.48

#### APERTURE EFFECTS AND ABERRATIONS

It has been shown that the focussed beam profile is that of the raw beam if aperture effects are neglected, and so the spot size will be given by the characteristic radius multiplied by the mode factor. The integral in (4) was calculated numerically to show the effect of a finite aperture on the spot size for the low order modes. The results are shown in table 2.

TABLE 2  
Increase in spot size due to finite aperture

a/w	m=0,n=0	m=0,n=1	m=1,n=0	m=1,n=1
0.5	2.55	2.87	1.64	2.04
1.0	1.37	1.61	1.55	1.28
2.0	1.00	1.00	1.00	1.00

It can be seen that if the aperture radius is greater than twice the characteristic radius of the beam then the effect is negligible.

Aberrations can be accounted by including an extra factor

$$\exp(ikW(r,\theta)) \quad (9)$$

in (4),  $W$  is the aberration function /5/ and describes the deviation of the actual wavefront from a spherical wavefront. For example,

$$W(r,\theta) = Cr^2 \quad (10)$$

describes spherical aberration.  $C$  depends on the amount of aberration present. Since the beam extends over a wider range for higher order modes, it would be expected that higher order modes would be affected more by aberrations.

#### THE EFFECTS OF MODE STRUCTURE ON LASER WELDING

Having detailed the relationship between the raw beam and the focussed beam, it is now possible to investigate the effects of mode structure using a three dimensional finite difference model /6/ adapted to accept any axisymmetric mode.

It is well known that weld width increases and penetration increases as the spot size of the laser beam increases. It is there-

There is to be expected that the weld width would be increased and penetration decreased by using a higher order mode, since the effective spot size would be greater.

In order to see if the actual mode structure itself has an effect the model was run for a TEM01\* mode and for a Gaussian mode of the same effective radius, as well as a Gaussian beam of the same characteristic radius, table 3

TABLE 3  
Effects of mode structure on weld profile  
(all lengths in mm)

	P= w=	1600W 0.25		2000W 0.50	
		w	d	w	d
TEM01*	w	0.8	1.7	2.0	1.4
TEM00	w	-	-	1.8	2.0
TEM00	1.32w	0.8	2.2	2.3	2.0

It can be seen that the TEM01\* beam has less penetration than a Gaussian of the same effective radius. This suggests that the mode structure does have an effect apart from just its increase in size, but it is felt that further investigation is necessary.

#### EXPERIMENT

Experiments are in progress at Imperial College to validate the ideas expressed in this paper. The experiment simply consists of placing an ALL Laser Beam Analyser in the path of a beam from a Control Laser Ltd. 2kW CO laser, so that the mode structure of the raw beam can be monitored while welding is carried out.

The ALL beam analyser can also be used to measure the focussed beam profile, and this will be used to check the relationship between the raw and focussed beams.

#### REFERENCES

1. DULEY, W.W. CO Lasers effects and applications Academic press 1976
2. READY, J.F. Effects of high power laser radiation  
Academic press 1971
3. KOGELNIK, H. & LI, T. Proc IEEE 54 1312 1966
4. BORN, M. & WOLF, E. Principles of optics Pergamon
5. LONGHURST, R.S. Geometrical and physical optics Longmans 1967
6. HENRY, P. et al Proc ICALEO 1982 Laser Institute of America

## APPENDIX D.

### A TWO-DIMENSIONAL TRANSIENT MODEL FOR CONVECTION IN LASER MELTED POOLS

by T. S. Mazumder\*\* and M. M. Chen\*\*\*

Department of Mechanical Engineering

University of Illinois at Urbana-Champaign

Urbana, Illinois

#### ABSTRACT

A two-dimensional transient model for convective heat transfer and surface tension driven fluid flow is developed. The model describes the transient behavior of the heat transfer process of a stationary band source. Some semi-quantitative understanding of scanning is obtained by a co-ordinate transformation. The non-dimensional form of the equations are derived and four dimensionless parameters are identified, namely, Peclet number (Pe), Prandtl number (Pr), Surface tension number (S), and dimensionless melting temperature ( $T_{melt}^*$ ). Their governing characteristics and their effect on pool shape, cooling rate, velocity field and solute redistribution is discussed. Numerical solution is obtained and presented.

#### NOMENCLATURE

C	constant which defines the interface; no unit, dimensionless
d	diameter of laser beam; mm, [L]
$D_{eff}$	effective diffusion coefficient; $m^2/sec$ , [ $L^2/t$ ]
k	thermal conductivity; $kW/m^{\circ}K$ , [ $M/Lt^2T$ ]
L	length of the rectangular heat source; mm, [L]
p	pressure; $N/m^2$ , [ $M/t^2L$ ]
Pe	Peclet number $u_0 d/k$ ; no unit, dimensionless
q	net heat flux from laser; $kW/mm^2$ , [ $M/t^2$ ]
Re	Reynolds number $u_0 d/v$ ; no unit, dimensionless

$r_0$	radius of laser beam; mm, [L]
S	Surface tension number; no unit, dimensionless
T	temperature; $^{\circ}K$ , [T]
$T_{melt}$	melting temperature; $^{\circ}K$ , [T]
$T_{melt}^*$	Dimensionless melting temperature $(\frac{T_{melt} - T_{metal}}{q d / K})$ ; no unit, dimensionless
$T_{metal}$	temperature of metal when it is not heated; $^{\circ}K$ , [T]

$\underline{u}$	velocity vector; mm/sec, [L/t]
u	x-component of $\underline{u}$ ; mm/sec, [L/t]
$u_0$	scanning speed of the laser beam; mm/sec, [L/t]
v	y-component of $\underline{u}$ ; mm/sec, [L/t]
w	z-component of $\underline{u}$ ; mm/sec, [L/t]
x, y, z	Cartesian coordinate; mm, [L]

#### Greek

$\rho$	density; $kg/m^3$ , [ $M/L^3$ ]
$\alpha$	thermal diffusivity; $m^2/sec$ , [ $L^2/t$ ]
$\nu$	kinematic viscosity; $m^2/sec$ , [ $L^2/t$ ]
$\mu$	viscosity; $kg/sec-m$ , [ $M/t-L$ ]
$\sigma$	surface tension, $N/m$ , [ $M/t^2$ ]

\* Graduate Research Assistant

\*\* Assistant Professor

\*\*\* Professor

1. *Journal of the American Medical Association*, 1997; 277: 1039-1043.

1. The liquid metal is considered to be Newtonian so that the Navier-Stokes equation is applicable.
2. All the properties of the liquid metal and solid metal are constant, independent of temperature (except the surface tension). This allows simplifications of the model; however, variable properties can be treated with slight modifications. The dependence of surface tension on temperature, the driving force of the flow, is assumed to be linear.
3. Latent heat of fusion is neglected since the energy liberated is small compared to total enthalpy change associated with temperature differences.
4. Thermal conductivity is assumed to be the same for both liquid and solid phases for the sake of simplicity of the model.
5. Surface of the melt pool is assumed to be flat, to simplify the surface boundary condition and, hence, surface rippling is neglected.

### MATHEMATICAL FORMULATION

Energy equation,

Continuity.

Momentum equations.

$$\partial v / \partial t + (u \cdot \nabla) v = -(1/\rho)(\partial p / \partial y) + \nu \nabla^2 v \quad (4)$$

$$y = 0, \quad v = 0, \quad u(\partial u / \partial y) = -\sigma'(\partial T / \partial x)$$

$$k(\partial T / \partial y) = \begin{cases} -q, & x \leq d \\ 0, & \text{otherwise} \end{cases} \quad (5)$$

$$f(x,y) = \text{constant}; u = v = U, T = T_{\text{me}}, \quad (6)$$

A two-dimensional analysis is presented, modeling a band source laser beam having a defined power distribution striking the surface of an opaque material of infinite width, thickness, and length (Fig. 1). Some of the incident radiation is reflected while the rest is absorbed. The heat absorbed developed a molten pool. Owing to the high temperature gradient on the surface in the transverse direction, the surface tension gradient is developed. It is this mechanism that drives the flow. As the flow develops, energy transfer mechanism becomes a convection problem with the flow driven by the surface tension gradient. The basic assumptions are:

*Journal of Management Education* 30(6)p.789-804  
© The Author(s) 2006. Reprints and permissions:  
<http://www.sagepub.com/journalsPermissions.nav>

$$\frac{\partial U}{\partial t} + u \frac{\partial U}{\partial x} + v \frac{\partial U}{\partial y} = \frac{\partial F}{\partial x} + \frac{\partial T}{\partial y} - \gamma^2 U \quad (11)$$

$$\frac{\partial v^*}{\partial t^*} + u^* \frac{\partial v^*}{\partial x^*} + v^* \frac{\partial v^*}{\partial y^*} = -\frac{\partial p^*}{\partial y^*} + \frac{\rho_r}{\rho_s} \gamma^* v^* \quad (12)$$

subject to the boundary conditions,

$$\text{at } y^* = 0, v^* = 0, \text{ S } \frac{\partial I^*}{\partial x^*} = - \frac{\partial U^*}{\partial y^*}$$

$$\frac{\partial T^*}{\partial y^*} = \begin{cases} -1 & |x^*| < 1/2 \\ 0 & \text{otherwise} \end{cases} \quad (13)$$

and at the liquid-solid interface,

$$f^*(x^*, y^*) = \text{Const.} \quad (14)$$

$$u^* = v^* = 0, \quad I^* = I^*_{\text{meit}}$$

and

$$|x^*|, y^* \rightarrow \infty, T^* \rightarrow 0 \quad (15)$$

where

$$Pe = u_0 d/\kappa, \quad Pr = \nu/\kappa \quad (16)$$

$$S = \frac{\sigma' q d}{u u_0 k}, T_{\text{melt}}^* = \frac{T_{\text{melt}} - T_{\text{metal}}}{q d / k}$$

It is important to point out that the four dimensionless parameters, namely  $Pe$ ,  $Pr$ ,  $S$  and  $T^*$ , are independent. They arise naturally from the general three-dimensional equations. However, in the case of two-dimensional heat source, there is a degeneracy. Reynolds number and surface tension number can be grouped together, their product as one parameter. We consider these four dimensionless parameters to understand the convection in the pool. This particular way of nondimensionalizing the equations also permit a simple transformation to obtain the scanning process.

100

The above information was not employed. The information was not presented in a form that would be of any particular use, however, the information is presented.

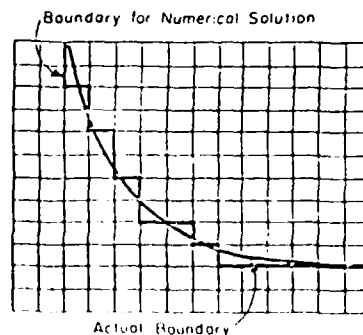
1. The first step is to identify the variables that are being measured. In this case, the variables are the number of people who are employed, the number of people who are unemployed, and the total number of people in the labor force.

[illegible]

$$\begin{aligned}
 FTY = & \frac{1}{4\delta y} \{ (v_{1,j}^n + v_{1,j+1}^n) (T_{1,j}^n + T_{1,j+1}^n) \\
 & + \alpha |v_{i,j}^n + v_{i,j+1}^n| (T_{i,j}^n - T_{i,j+1}^n) \\
 & - (v_{i,j-1}^n + v_{i,j}^n) (T_{i,j-1}^n + T_{i,j}^n) \\
 & - \alpha |v_{i,j-1}^n + v_{i,j}^n| (T_{i,j-1}^n - T_{i,j}^n) \} \quad (19)
 \end{aligned}$$

$$\begin{aligned} TIS = & \frac{1}{pe} \left\{ \frac{1}{\partial x^2} (T_{i+1,j}^n - 2T_{i,j}^n + T_{i-1,j}^n) \right. \\ & \left. + \frac{1}{\partial y^2} (T_{i,j+1}^n - 2T_{i,j}^n + T_{i,j-1}^n) \right\}. \end{aligned} \quad (20)$$

The second modification is the irregular boundary of the interface. It is approximated by steps of grids that are closest to the interface (see Fig. 2).



There is a lot of information out there, and it is important to know how to use it. The first step is to identify the problem you are trying to solve. Then, you need to gather information about the problem. This can be done by reading books, articles, and websites. Once you have gathered information, you need to analyze it. This means looking at the information and trying to understand it. Finally, you need to use the information to solve the problem. This can be done by applying the information to the problem and seeing if it works.

The numerical solution for the problem is first carried out for a fixed value of the surface tension number. The value of the surface tension number is then varied and the solution is repeated. The value of the surface tension number is varied in such a way that we have an effect on the shape of the molten pool. The value of the surface tension number is varied in such a way that we have an effect on the shape of the molten pool. The value of the surface tension number is varied in such a way that we have an effect on the shape of the molten pool.

The numerical solution for the problem is first carried out for a fixed value of the surface tension number. The value of the surface tension number is then varied and the solution is repeated. The value of the surface tension number is varied in such a way that we have an effect on the shape of the molten pool. The value of the surface tension number is varied in such a way that we have an effect on the shape of the molten pool.

#### DISCUSSION OF THE MODEL

The governing parameters which enter the dimensionalized equations are Reynolds number ( $Re$ ), Prandtl number ( $Pr$ ), surface tension number ( $S$ ), and dimensionless melting temperature ( $T_{melt}^*$ ). Each of these would govern the characteristics of the problem and each has its own physical interpretation.

Peclet number can be interpreted as the ratio of heat diffusion time to scanning interaction time. Reynolds number is the quotient of Reynolds number and Prandtl number. The latter is a property of the molten material--the ratio of momentum diffusion and the

The numerical solution for the problem is first carried out for a fixed value of the surface tension number. The value of the surface tension number is then varied and the solution is repeated. The value of the surface tension number is varied in such a way that we have an effect on the shape of the molten pool. The value of the surface tension number is varied in such a way that we have an effect on the shape of the molten pool.

The numerical solution for the problem is first carried out for a fixed value of the surface tension number. The value of the surface tension number is then varied and the solution is repeated. The value of the surface tension number is varied in such a way that we have an effect on the shape of the molten pool. The value of the surface tension number is varied in such a way that we have an effect on the shape of the molten pool. The value of the surface tension number is varied in such a way that we have an effect on the shape of the molten pool.

Table 1 Physical Property of Steel, Al, and  $NaNO_3$

	Steel	Al	$NaNO_3$
$\rho$	$7.0 \times 10^3 \text{ kg/m}^3$	$2.385 \times 10^3 \text{ kg/m}^3$	$1.904 \times 10^3 \text{ kg/m}^3$
$\mu$	$5.6 \times 10^{-3} \text{ N s m}^{-2}$	$2.8 \times 10^{-3} \text{ N s m}^{-2}$	$+2.78 \times 10^{-3} \text{ N s m}^{-2}$
$\nu$	$7.84 \times 10^{-6} \text{ m}^2/\text{sec}$	$1.17 \times 10^{-6} \text{ m}^2/\text{sec}$	$1.46 \times 10^{-6} \text{ m}^2/\text{sec}$
$k$	$31 \text{ W/m}^\circ\text{K}$	$100 \text{ W/m}^\circ\text{K}$	$1.0 \times 10^{-5} \text{ W/m}^\circ\text{K}$
$K$	$1.0 \times 10^{-5} \text{ m}^2/\text{sec}$	$6.0 \times 10^{-5} \text{ m}^2/\text{sec}$	$5.6 \times 10^{-7} \text{ m}^2/\text{sec}$
$T_{melt}$	$1500^\circ\text{C}$	$600^\circ\text{C}$	$306.8^\circ\text{C}$
$\sigma'$	$-0.112 \times 10^{-3} \text{ N/m}^\circ\text{K}$	$-0.35 \times 10^{-3} \text{ N/m}^\circ\text{K}$	$-0.7 \times 10^{-4} \text{ N/m}^\circ\text{K}$

Table 2 Order of Magnitude of Parameters

	Steel	Al	$NaNO_3$
$Re$	2.55 to 8.29	17 to 55	14 to 45
$Pe$	2 to 6.5	0.3 to 1.0	36 to 120
$S$	$5 \times 10^4$ to $2.5 \times 10^5$	$10^5$ to $5 \times 10^5$	$2.0 \times 10^8$ to $10^9$
$T_{melt}^*$	0.005 to 0.001	0.006 to 0.016	$3 \times 10^{-10}$ to $7 \times 10^{-10}$

As a result, the model is able to capture the essential features of the data, and the results are more reliable and accurate than those obtained from traditional methods.

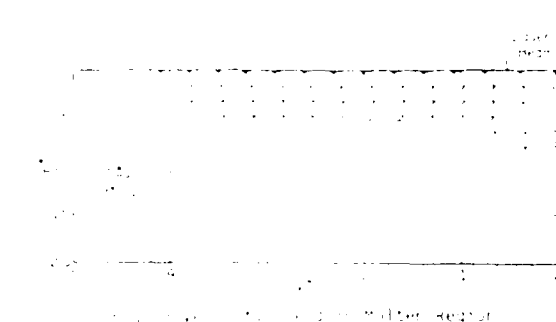
[illegible]

### 3. Surface Temperature

The surface temperature within the molten region, for different surface tension numbers and Prandtl numbers are plotted in Fig. 8 and 9 respectively. The curve exhibits the usual feature, it attains its maximum at the center and decreases as it moves to the edge. The temperature gradient, driving force of the fluid flow, is greatest at the edge of the laser beam ( $x^* = 0.5$ ). The effect of surface tension number on the surface temperature, as can be seen in Fig. 8, is rather small as compared to the effect of Prandtl number on it. Fig. 9 Prandtl number, as explained earlier, is the ratio of momentum and thermal diffusivity. An increase in Prandtl number can be interpreted as a decrease in thermal diffusivity. Thus, the material is heated up more slowly when its Prandtl number is higher. As can be seen in Fig. 9, the temperature gradient decreases with Prandtl number. This causes the magnitude of the recirculating flow decrease with Prandtl number.

### C. Horizontal Surface Velocity

The horizontal surface velocity at  $t^* = 1$  and  $x^* = 0.5$  as a function of S number is plotted in Fig. 10. The magnitude increases with S number which is expected. The horizontal surface velocity at  $t^* = 1$  and  $x^* = 0.5$  as a function of Pr number is plotted in Fig. 11. The velocity decreases with the Prandtl number. As explained earlier, this is due to the decrease in temperature gradient.



1. *Journal of the American Medical Association*, 1997; 277: 1033-1038.

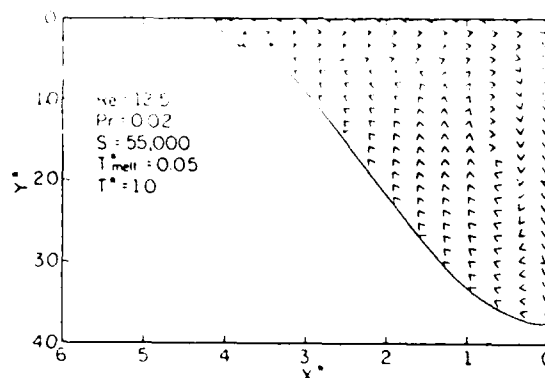


Fig. 4 Velocity Field in Molten Region

Table 3 Value of the Governing Parameters of the Five Cases

Case	1	2	3	4	5
Re	12.5	12.5	12.5	12.5	12.5
Pe	1.25	0.25	32.5	1.25	1.25
Pr	0.1	0.02	2.6	0.1	0.1
S	55,000	55,000	55,000	30,000	55,000
$\sigma_{\text{max}}$	1.0	1.0	1.0	1.0	1.0



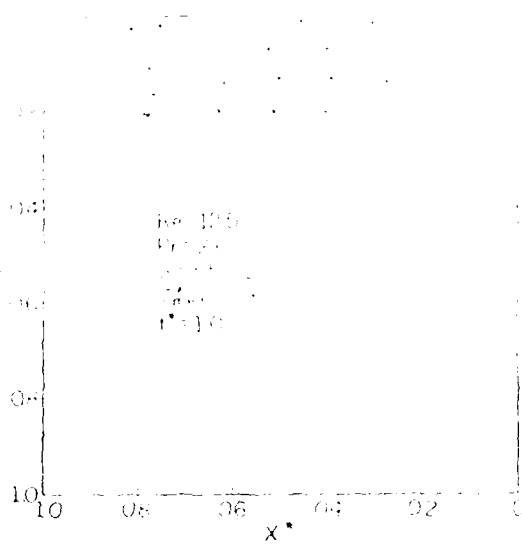


Fig. 5 Velocity field in Molten Region

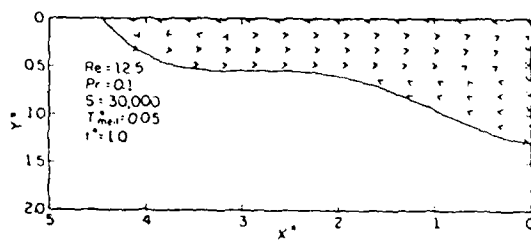


Fig. 6 Velocity field in Molten Region

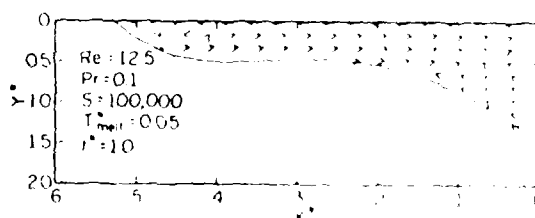


Fig. 7 Velocity field in Molten Region

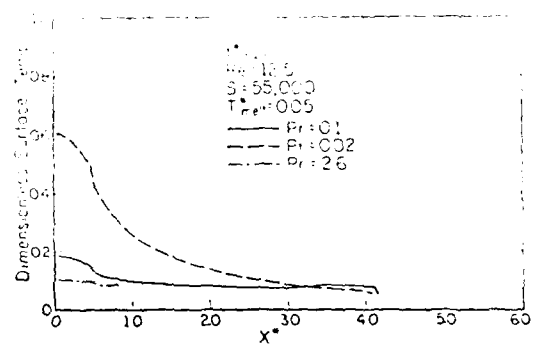


Fig. 9 Surface Temperature for Different  $Pr$

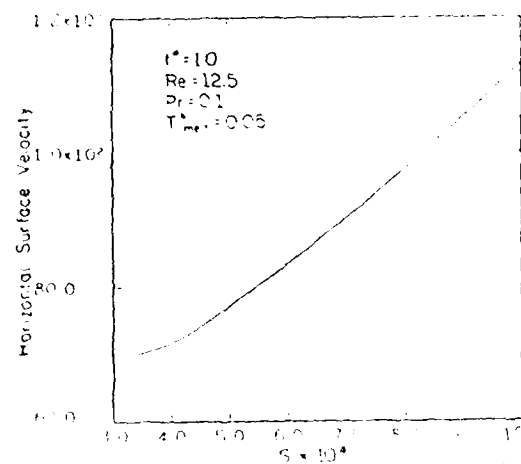


Fig. 10 Horizontal Surface Velocity versus Surface Tension Number

As the Prandtl number increases, the heat becomes more difficult to diffuse. Therefore, the size of the molten region decreases. Moreover, the Grashof number (product of Reynolds number and Prandtl) would also increase. As a result, the convection becomes more and more important. This is reflected by the fact that the aspect ratio (width divided by depth), as plotted in Fig. 15, increases with the Prandtl number.

#### E. Cooling Rate

The cooling rate along the interface of the first case is plotted in Fig. 16. The cooling rate is calculated from Eq. (9). The cooling rate increases as one moves away from the bottom (center), then it attains a local maximum and decreases, finally it increases to the edge of the pool. The existence of the local maximum is unusual, but expected. The reason is because of the existence of the two counter rotating vortex. The cooling rate attains its local maximum at the location where the two vortex meet. In all five cases, the cooling rate at the edge of the pool is higher than that at the bottom (center) of the pool. Thus, the molten region, as it solidifies, would shrink faster in its width than its depth. This predicted trend is consistent with the experimental fact that the microstructure is finer at the edge of the pool than at the bottom of the pool. The cooling rate at the edge of the pool as a function of  $S$  number and  $Pr$  number are plotted in Figs. 17 and 18, respectively. The cooling rate increases with the  $S$  number since higher the  $S$  number, higher the convection and thus more efficient is the heat transfer. The cooling rate increases at first and then decreases with  $Pr$  number. The reason behind is that there are two parts in the cooling rate, convection and conduction. For small  $Pr$  number, conduction is dominating so that an increase in  $Pr$  number decreases the conduction and thus the cooling rate. On the other hand, where  $Pr$  number is large, convection is more important. Convection increases with  $Pr$  number, hence more efficient heat transfer. As a result, the cooling rate increases.

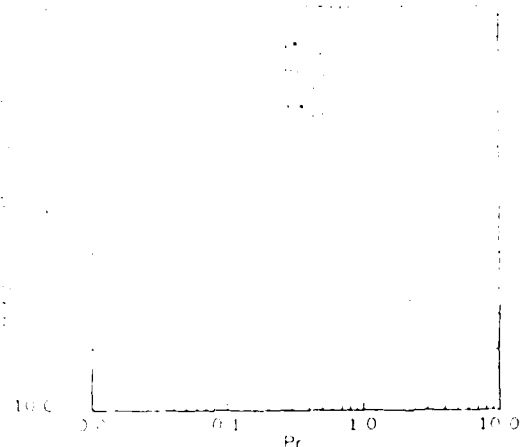


Fig. 11 Horizontal Surface Velocity versus Prandtl Number

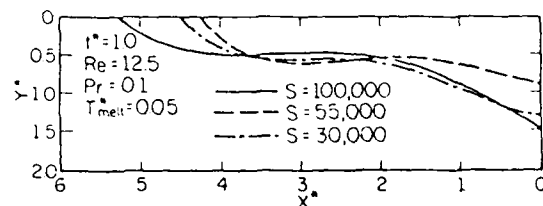


Fig. 12 Molten Region at  $t^* = 1.0$  for Different  $S$

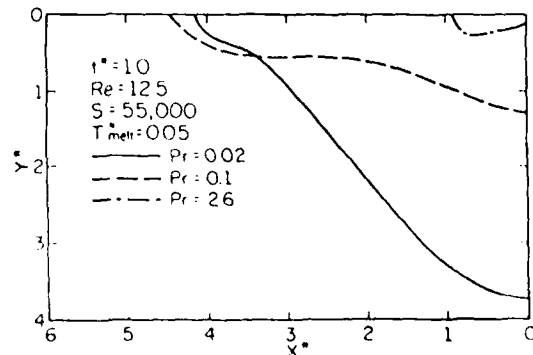


Fig. 13 Molten Region at  $t^* = 1.0$  for Different  $Pr$

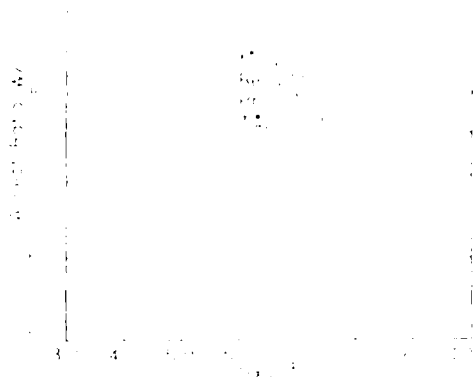


Fig. 14 Graph of Aspect Ratio versus Surface Tension Number

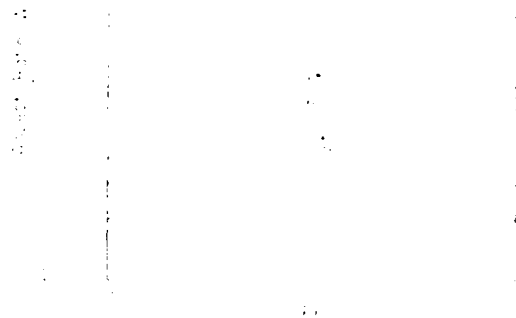


Fig. 15 Graph of Aspect Ratio versus Prandtl Number

#### F. Solute Redistribution

The recirculating velocity, as predicted by this model, is of one or two orders of magnitude higher than the scanning speed. This means a fluid particle would recirculate several times before it solidifies. This can account for the highly disperse and uniform solute redistribution within the molten region. The transport process is convection dominated. The solute is actually transported by the carriage of the flowfield, molecular diffusion play a rather subordinate role. Because of the fact that there are two counter rotating vortex, one would expect to have segregation, if any, at the location where the vortex meet.

#### CONCLUSIONS

This two-dimensional convective heat transfer and fluid flow analysis has revealed many important aspects of the surface tension driven fluid flow in weld pool and its effect on pool shape, cooling rate, velocity field and solute redistribution. The important findings are as follows:

1. Recirculating velocity is predicted with the flow one or two order of magnitude higher than that of the moving heat source. There are two counter rotating vortexes except in the high Prandtl number (2.6) case.
2. Surface temperature gradient, which is the driving force for the fluid flow, is maximum at the edge of the beam leading to the most rigorous outward velocity.
3. As Prandtl number increases, the aspect ratio (width divided by depth) increases.
4. As surface tension number increases from 30,000 to 50,000, the aspect ratio increases. However, when it increases from 55,000 to 100,000, the aspect ratio decreases leading to "key-hole" mode penetration due to the counter rotating vortex.
5. The cooling rate at the edge of the pool is found to be higher than that at the bottom of the pool below the centerline. This implies the solidification will proceed from the edge of the pool.

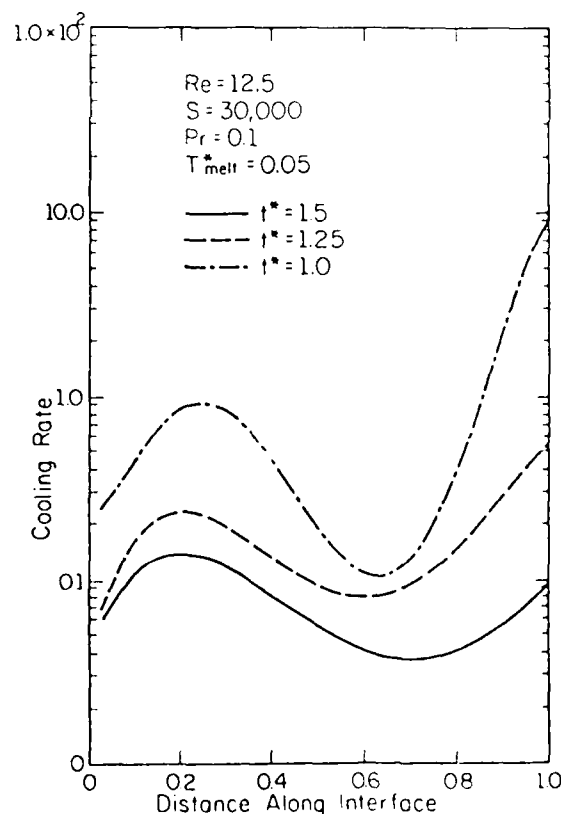


Fig. 16 Cooling Rate along Interface for Different  $t^*$

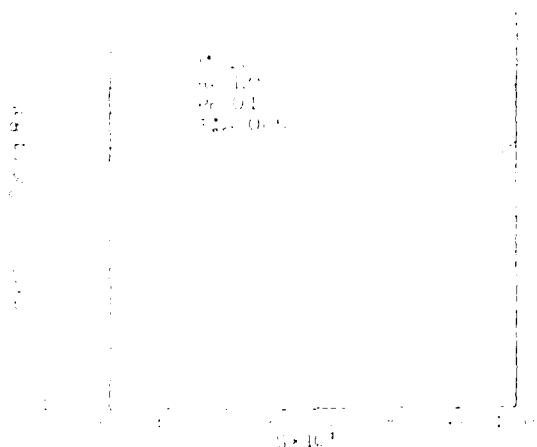


Fig. 15 Graph of Cooling Rate at Pool Edge versus Surface Tension Number

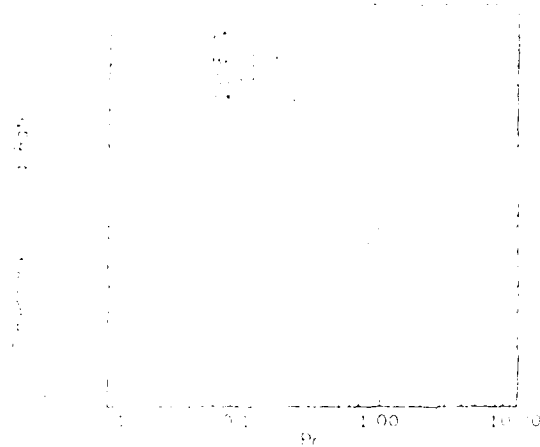


Fig. 16 Graph of Cooling Rate at Pool Edge versus Prandtl Number

6. As Prandtl number increases from 0.02 to 0.1, the cooling rate at the edge of the pool decreases. But it increases when the Prandtl number increases from 0.1 to 2.6.
7. The cooling rate at the edge of the pool increases with the surface tension number.
8. Because of the high recirculating flow, uniform solute redistribution is expected. The existence of the counter rotating vortexes in the pool implies some segregation, if any, can be expected at the location where the vortexes meet.

#### ACKNOWLEDGEMENTS

This work was partially funded by a grant from American Iron and Steel Institute Grant No. AISI 62-443.

#### REFERENCES

1. D. S. Gnanamuthu, Applications of Lasers in Materials Processing, E. A. Metzbower, ed., ASM, Metals Park, OH, 1979, pp. 177-289.
2. P. M. Moore, and L. S. Weiman, Proc. Soc. of Photo-Opt Instrum. Eng., 1979, Vol. T98, p. T20.
3. L. S. Weiman, J. H. Devault, and P. Moore, Applications of Lasers in Materials Processing, E. A. Metzbower, ed., ASM, Metals Park, OH, 1979 pp. 245-259.
4. C. W. Draper, Proc. Conf. of Lasers in Metallurgy, K. Mukherji and J. Mazumder, eds., AIME, Warrendale, PA, 1981.
5. L. S. Weiman, and J. H. Devault, AIP Conference Proc. No. 50, Symp. on Laser Solid Interactions and Laser Processing, Boston, Mass., 1978, p. 239.
6. T. R. Anthony, and H. F. Cline, J. Appl. Phys., 1977, Vol. 48, No. 9, pp. 3848-3894.
7. T. Chande, and J. Mazumder, Appl. Phys. Letter, 1982, Vol. 41, No. 1, p. 42.
8. C. R. Heiple, and J. R. Roper, Welding Journal, 1982, Vol. 61, pp. 973-1025.
9. C. W. Hirt, B. D. Nichols, and N. C. Romero, "A Numerical Solution Algorithm for Transient Fluid Flows," UC-34 and UC-79d, April 1975.
10. C. Chan, J. Mazumder, and M. M. Chen, to appear in Applications of Lasers in Materials Processing, E. A. Metzbower, ed., ASM, 1983.
11. P. T. Houldcraft, British Welding J., 1954, Vol. 1, 468.
12. W. I. Pumphrey, British Welding J., 1955, Vol. 2, p. 93.
13. R. A. Woods, and D. R. Milner, "Motion in the Weld Pool in Arc Welding," Welding J., 1971, Vol. 50, No. 4, pp. 163s-173s.
14. C. R. Heiple, J. R. Roper, R. T. Stagner, and R. J. Aden, Welding J., 1983, Vol. 62, pp. 72s-77s.
15. A. L. Shaeffler, "Selection of Austenitic Electrodes for Welding Dissimilar Metals," Welding J., 1947, Vol. 25, No. 7, pp. 601s-620s.
16. R. L. Apps, and D. R. Milner, British Welding J., 1963, Vol. 10, p. 348.
17. R. L. Apps, and D. R. Milner, British Welding J., 1955, Vol. 2, p. 475.
18. N. Christensen, V. de L. Davies, and K. Gjermundsen, British Welding J., 1965, Vol. 12, p. 54.
19. R. J. Bradstreet, "Effect of Surface Tension and Metal Flow on Weld Bead Formation," Welding J., 1968, Vol. 47, No. 7, pp. 314s-322s.
20. G. R. Salter, and D. R. Milner, British Welding J., 1960, Vol. P44.
21. G. R. Salter, and D. R. Milner, British Welding J., 1965, Vol. 12, p. 222.
22. D. Howden, and D. R. Milner, British Welding J., 1965, Vol. 12, p. 222.
23. T. Chande, and J. Mazumder, Metallurgical Transaction, 1983, Vol. 14B, pp. 181-190.

# RANGE OF RAPID SOLIDIFICATION STRUCTURES WITH LASER SURFACE TREATMENT OF SPECIAL STEELS

G. Christodoulou, P. Henry, W.M. Steen

Imperial College of Science and Technology,  
London, England.

## SUMMARY

Four different steels each having two different prior heat treatments, were surface melted with a laser of 1.7kW and various traverse speeds and beam diameters.

The experimental results are described, together with some preliminary mathematical modelling.

## INTRODUCTION

The use of a laser to produce rapidly solidified structures in the surface of different materials has recently received considerable attention (1,2). This is principally because it is one of the few methods available for producing these interesting structures on the surface of articles of use in engineering, such as wear surfaces.

The current level of research is aimed at categorising what structures can be obtained, with some work on detailed structural analysis (3) and others on their engineering properties such as wear resistance, corrosion resistance, and fatigue resistance (4).

Discussed here are the structures obtained by traversing a laser over four different steels.

## EXPERIMENTAL

A Control Laser 2kW CW CO<sub>2</sub> laser was used. The laser power output was fixed at 1.7kW and passed with various beam diameters over four different steels whose compositions were:-

The steels were received in two states, the fully austenitised condition and the fully heat treated condition; except for the S82 which was surface carburised to around 1mm depth and then heat treated at 100°C for 4 hours or 140°C for 4 hours.

The range of traverse speeds explored was from 8mm/s to 1200mm/s while the beam diameter (defocused Gaussian beam) was varied from 0.2mm (focus) to 4.3mm.

## RESULTS AND DISCUSSION

The results were examined to establish:

- 1) The dimensions of the laser treated zone
- 2) The solidification mechanism
- 3) The Crystal structure
- 4) The extent of any surface modification and upset.

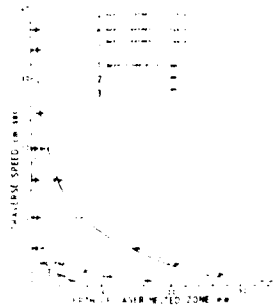
### THE DIMENSIONS OF THE LOWER TREATED ZONE

The variation of depth and width of the melted zone is shown in fig.1 and 2. The laser coupling varies from deep penetration by "keyhole" formation to conduction limited melting and surface transformation hardening with no surface melting (5).

It is apparent from fig.1 and 2 that the prior heat treatment had no effect on the melt zone, neither did it change the size of the heat affected zone. There is only slight variation between the steels with the S99 being a little more difficult to penetrate. The hyperbolic relationship between speed and

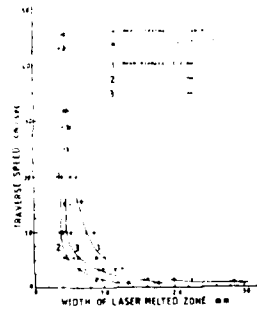
Material	C	Si	Mn	S	P	Ni	Cr	V	Mo
S82	0.14	0.23	0.35	0.005	0.005	4.03	1.09	-	0.26
S99	0.37	0.21	0.68	0.022	0.007	2.46	0.69	-	0.605
S99M	0.43	1.57	0.88	0.005	0.009	1.90	0.80	0.70	0.35
S135	1.0	0.29	0.42	0.01	0.007	0.17	1.39	0.02	-

Fig. 1:



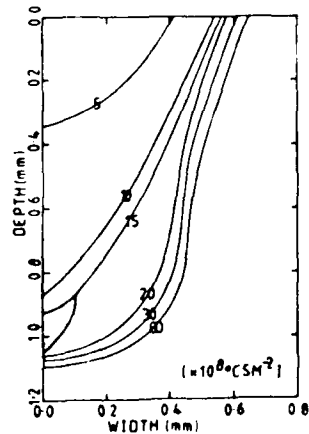
Variation of depth of laser melted zone with traverse speed for S135 Steel at three different heat treatment conditions and beam diameters.

Fig. 2:



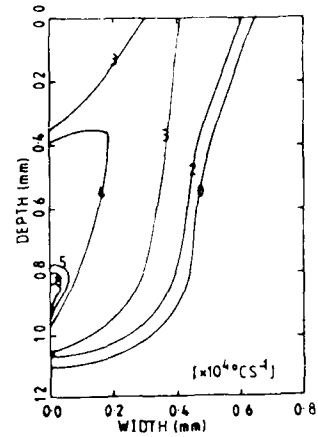
Variation of width of laser melted zone with traverse speed for S62 Steel at two different heat treatment conditions and three beam diameters.

Fig. 3:



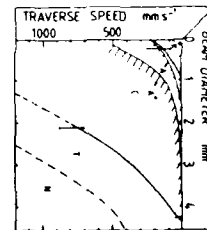
Theoretical G.R. ratio isobars for a weld exhibiting keyholing.

Fig. 4:



Theoretical G.R. ratio isobars for a weld exhibiting keyholing.

Fig. 5:



Structural map of surface carburised S82 Steel for a laser power of 1720W

- A- Area of possible retained austenite heat treatment 1.
- A\*- Area of possible retained austenite heat treatment 2.
- C- Conduction region
- C- Conduction limited melt zone
- T- Transformation hardening with no surface melting
- N- No visible effects
- P- Porosity and cracking

penetration is expected by simple heat balance calculations. The reasoning, based on heat conduction leads to the conclusion that keyholing occurs if:

$$P/VD \geq 60 \pm 20 \text{ J/mm}^2$$

conduction: limited melting if  $60 \pm 20 \leq P/VD \leq 2 \pm 1 \text{ J/mm}^2$  and transformation hardening if  $2 \pm 1 \leq P/VD \leq 0.7 \pm 0.4 \text{ J/mm}^2$  where P = incident power W, D = beam diam, mm, V = traverse speed mm/s.

#### SOLIDIFICATION MECHANISM

Solidification is by a dendritic, or cellular dendritic growth. Fig. 3 shows a theoretical calculation for a keyhole melt of the thermal gradient G divided by the solidification rate R (G/R ratio) which has been considered related to the stability of various solidification mechanisms (6). A considerable variation in value is calculated particularly at the chill edge, giving the possibility of a thin equiaxed zone, leading to a dendritic core with a tendency towards cellular dendritic growth towards the centre surface. Fig. 4 also for a keyhole melt is a plot of the cooling rate (G.R) over the melt zone. This parameter has been noted (6) to be correlated to the dendrite arm spacing. This particular calculation suggests a variation in arm spacing with a finer arm spacing at the centre of the keyhole and the central surface, observed values in a comparable keyhole run vary from  $\mu\text{m}$  to  $\mu\text{m}$ . For this calculation it was assumed that the dendrites grew along the maximum thermal gradient, but examination of dendrite growth directions showed that although basically following the predicted direction there were notable exceptions which must be due to convective movement within the melt.

Some solidification cracking and blind weld porosity was observed in the deeper keyhole samples. Fig. 5 is a structural map of the S82 steel.

#### CRYSTAL STRUCTURE

Optical microscopy showed martensite and a white etching retained austenite. The hardness figures were used to confirm these structures.

The high C, low Si and V steels favoured retained austenite at the faster processing speeds. The 300M steel did not show any retained austenite.

The S135 steel showed an unusual banded structure which is apparently molten since the surface had moved in some samples but was apparently not

molten since the bands follow a pattern right up to the surface internally. The bands are considered to have been partially molten due to the large differences between solidus and liquidus in this 1-C steel.

#### SURFACE PROFILE

By using larger beam diameters smooth surfaces were obtained.

#### CONCLUSION

Data on the dimensions of laser treated zones are given, together with preliminary mathematical predictions of the solidification mechanism. The crystal structure is martensite with some retained austenite in the high C low Si and V steels.

#### REFERENCES

1. B.H. Kear, E.M. Breinan L.E. Greenwald and C.M. Banas, Tech. paper M.R. 76-867, 1976.
2. S.M. Copley, D. Beck, O. Esquivel and M. Bass, "Laser-Solid Interactions and Laser Processing" p161, edited by S.D. Ferris and H.J. Leamy and J.M. Poate, American Institute of Physics, New York 1979.
3. B.G. Lewis, D. Gilbert, and P.R. Strutt, "Processing and Properties of High Speed Tool Steels", p84, Conf. Proc. AIME Las Vegas Feb. 1980, Publ. Metal. Soc. AIME, Warrendale Pa.
4. T.R. Anthony and H.E. Cline, J. Appl. Phys. p1298 vol. 49, No.3, March 1978.
5. G. Christodoulou and W.M. Steen, "Laser '81 Conf. Munich 1981 to be published.
6. M.C. Flemings "Solidification Processing", p75-76 & 146-154 McGraw Hill, New York 1974.

## APPENDIX F

### COMPUTER SIMULATION MODEL FOR LASER CLADDING

BY

V. M. Weerasinghe and W. M. Steen

Metallurgy Department, Imperial College, London

ASM MEETING

BOSTON

NOV 1983.

#### ABSTRACT

The process of laser cladding using gas borne injected powder has already achieved industrial acceptance. The cladding material in the form of a fine powder is injected into the laser generated melt pool on a moving substrate. The present model is aimed at calculating the resulting clad weld bead dimensions and the temperature distribution in the heated zone. A simulation model is also presented for the overlapping of single clad tracks to produce layers of uniform thickness.

#### INTRODUCTION

Cladding is one of the many material processing applications for which a laser has been and is being used. Fig 1 illustrates the powder injection process, currently being used by Rolls Royce (1).



Fig 1. Laser cladding by powder injection.

The cladding material in the form of a fine powder (usually of non-spherical shape and average size of 70 microns) is injected into the laser-generated melt pool on the moving substrate. The other method of

laser cladding is by melting a pre-placed powder layer. The use of the cladding material in the form of a powder is preferred as an instantaneous layer of powder on or near the surface appears to enhance the laser energy coupling efficiency.

The mathematical model presented here is applicable to the injection process. The main parameters of this process and the effect of these parameters on the dependent parameters have been studied and reported elsewhere (2).

The model described here assumes a quasi-steady state with the axis of reference fixed relative to the laser beam, the beam being incident normal to the substrate and stationary with respect to the earth.

The beam is assumed parallel, with a mathematically defined power intensity distribution similar to that produced by a T.E.M.<sub>00</sub> mode. The spot radius is defined as the radial distance where the central intensity is reduced by a factor  $1/e$ .

The present model, although not lacking in generality, is aimed at co-relating experimental data obtained for flat plate cladding of stainless 316 to a mild steel EN3 substrate, using a 2 kw CO<sub>2</sub> laser.

The temperature dependence of some physical properties is allowed for. Effects due to latent heats are accounted. Heats generated by chemical reactions and 'body convection' due to melt pool turbulence are neglected.

A semi-spherical reflecting device was used to measure the total reflected power from a shot blasted mild steel surface. Fig 2. A reflectivity value of 0.4 was obtained for a normal incident CO<sub>2</sub> laser



intensity of  $1.3 \times 10^6 \text{ W/m}^2$ . As this intensity value represents an average for the various temperatures generated, a linear function varying from 0.8 at 300K to a limiting value of 1.3 at 1650K is used.

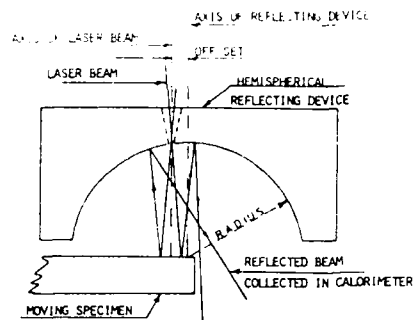


Fig 2. Measurement of the reflected beam power at normal incidence.

The powder particles are assumed to be of spherical shape. A weighted average value, based on a sieve analysis, is used for the particle diameter. An average measured value of 1.6 m/s is used for the particle velocity. For the loading ratios used, the particle distribution in the powder cloud is assumed to be uniform.

The temperature distribution in the clad bead and the surrounding heat affected zone is obtained by a finite difference heat balance.

#### PROPOSED CLADDING MECHANISM

Before the quasi-steady state is established, there is a transient period in which the clad bead is initiated. At time zero, the laser beam traverses through the powder cloud and impinges on the substrate. A fraction of the laser power is absorbed by the powder particles. The energy coupling efficiency may be enhanced by a fine powder layer on and near the substrate surface. A molten pool is quickly generated extending initially below the substrate surface. The incoming powder particles are then entrapped in the molten pool forming a clad bead above the surface. The solid/liquid interface will extend below the substrate surface if there is insufficient powder flow to match the laser power density, Fig 4. If there is excess powder flow, then the resulting clad bead would be smaller.

Some particles may be ejected out of the molten pool as is evident from a fast action cine film.



Fig 3. Effect of powder mass flow on surface reflectivity. (Top image is at 0.090 g/s, bottom image is at 0.212 g/s)



Fig 4. Effect of powder mass flow.  
Powder mass flow 0.090 g/s top  
0.212 g/s bottom

Criterion for successful cladding is melting of the substrate by conduction through the super heated clad bead molten pool. Microscopic examination of 70  $\mu\text{m}$  stainless steel particles which were injected through a 5 mm beam of 1830W, revealed no melting (i.e. no dendritic structure or rounding of sharp edges), Fig 5. Although some smaller particles present in a mixture may melt before arriving at the clad bead molten pool, pre-melting of the particles is not a criterion.



Fig 5. Microstructure and shape of stainless steel particles which were injected through a 5 mm beam of 1830W. 500 x

#### MODEL FOR THE MODEL

The model is based on the following experimental observations:

(a) The clad bead width is observed to be approximately equal to the width of the melt width produced on the substrate when there is no powder injection, the other parameters being the same. Different cladding materials ranging from chromium to brass seem to form beads of similar widths but of different heights when clad on the same substrate, provided no chemical reactions occur (e.g. excessive surface oxidation or formation of inter-metallic compounds), Fig 6.

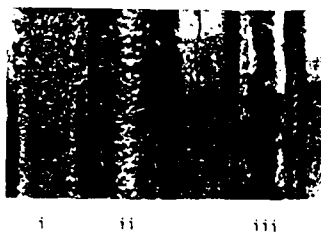


Fig 6. Similarity of substrate melt width (iii) and clad bead width (i,ii). Substrate mild steel, clad - (ii) Brass, (i) Stainless steel.

Beads of cladding materials with a higher melting point than the substrate, spread out to the full width of the substrate surface melt. If the energy input is insufficient to generate temperatures higher than the melting point of the clad, then individual particles are observed entrapped in the substrate molten pool. Similarity of the two widths will be greater for clad/substrate combinations with similar high temperature physical properties. Satisfactory cladding is not possible when the melting point of the clad is much higher than the substrate (2).

(b) The section profile of a single clad bead is a segment of a circle. This profile has been observed to be independent of all process parameters. Clad beads of stainless steel, iron, brass, stellite and nickel were examined.

Laser cladding is a comparatively calm process relative to plasma, flame or arc processes. There are no electro-magnetic forces or gas jets to disturb the molten pool. Also it is evident that there is little molten pool turbulence. This was verified by cladding pure iron to a stainless steel (18% Cr) substrate under conditions which would create a high dilution level. Although there was about 30% dilution, (i.e. 30% of the molten pool extending

into the substrate) the clad bead was observed to be flat from the substrate surface.

Under the above conditions, the clad profile may be expected to be a segment of a circle due to the symmetrical surface tension effects and controlled power input (Fig 7).



Fig 7. Three basic clad bead section profiles. Clad - Stainless steel, Substrate - Mild steel.

#### MODEL OUTLINE

Certain parameters are first calculated using an existing finite difference laser heating model (3) assuming no formation of a clad bead and no powder injection. These parameters are:

(c) Surface melt width and centreline melt length

(d) Surface melt area

(e) Position of the beam centre in the molten pool

(f) The length of the heated zone in the x,y,z direction: XR,YR,ZR.

The objective of the above calculation is to obtain a first estimation of the bead section profile.

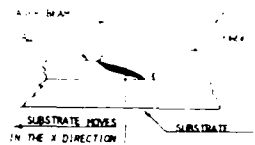
Observation (a) allows a first estimation of the clad bead width to be obtained using (c) above. A first estimation of the clad bead height is calculated by using (d) above, assuming that the clad bead is made from all the particles falling on to the molten pool area and by expressing the injected mass flow as mass flow per unit area.

A cartesian matrix is set up allowing sufficient grid points inside the estimated clad bead profile. The lengths of the heat affected zone calculated in (f) above, are used as initial limiting lengths.

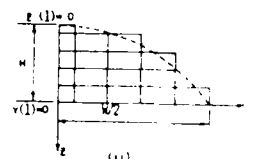
The power input to each surface element is then calculated using a procedure similar to that described in (3), i.e.:

$$POWER(K,I) = \iint_R P(x,y) dy dx$$

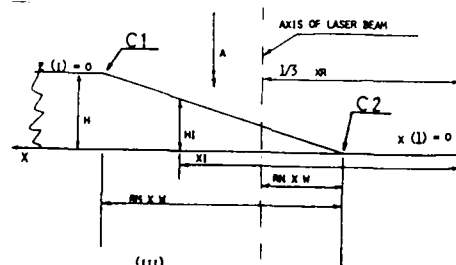
where 'R' is the region bounded by grid point (K,I) and  $P(x,y)$  is the power intensity distribution function.



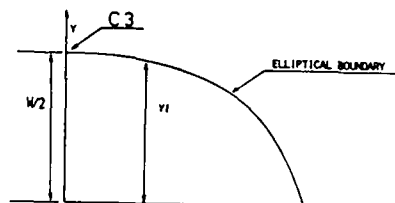
(i)



(ii)



(iii)



(iv)



Fig 8. Matrix set up. (i) General arrangement (ii) Clad bead body - transverse section (iii) Clad bead molten pool end - longitudinal section (iv) View 'A' of (iii), (v) Macrograph of (iii), (vi) Macrograph of (iv).

The shadowing effect of the particle cloud is evaluated for each surface grid point.

The progressive temperature rise of a powder particle traversing through the laser beam and falling on to a particular surface grid point is calculated for the various energy inputs en route, allowing for a forced convective loss due to the conveying gas flow and a radiative loss.

In the subsequent heat balance, the heat content of the particles is added to the respective surface grid points as a body convection term and the power input is adjusted according to the shadowing effect of the particles.

If the resulting temperature distribution does not satisfy certain criteria which depict the quasi-steady state of the molten pool, then the clad bead width and height are varied until a satisfactory distribution is obtained.

#### MATRIX SET UP - TEMP (K, I, L)

The circular bead section is modelled as a stepped cartesian grid as shown in Fig 8. Symmetry allows only one half of the bead to be considered. The boundary of the grid is defined by the bead radius. The front end of the clad track, i.e. the molten pool end, is modelled as follows: With reference to Fig 8(iii), the molten pool elongation factor 'RM' is calculated

Using information from (4), the initial half length width. If  $RM \times W$  is found to be that point C is outside the powder injection range. (Fig. 4), then  $RM \times W$  is limited to the powder injection range.  $RM \times W$  becomes large at high injection points. In the  $X$  direction,  $X$  is the distance from point C to the laser beam.  $W$  is the width of the substrate.  $RM \times W$  is limited to the powder injection range. The laser beam is projected from the nozzle used to locate the beam center relative to the molten pool. The bead radius is calculated at each section (e.g., using 'H1' as height and  $2Y1$  as width at  $X = X1$ ), and a stepped grid synchronous with the clad body grid is set up.

Twelve grid points are allowed in the  $X$  direction between C1 and C2. The total grid size is  $10 \times 3 \times 15$ .

#### THE SHADOWING EFFECT OF THE PARTICLE CLOUD - RLOSS (K,1)

Assuming a weighted average particle diameter, the number of particles per unit volume is first calculated. This is a function of the particle velocity, particle diameter, mass flow and injector tube diameter.

Fig 9 shows the powder cloud in relation to the laser beam. The powder cloud is considered to be of square section for the purpose of statistical analysis, a correction being made at a later stage.

The shadowing effect is evaluated as a percentage laser power loss for each surface element within the powder cloud. As the particle distribution is considered to be uniform, the problem is reduced to a single dimension, the effect being independent of the element location in the 'y' direction.

Reference to Fig 9, the instantaneous number of particles in the volume of space above each element is calculated. A two dimensional matrix is then set up, the matrix lengths being the element length in the  $x$ -direction and the cloud range in the  $y$  direction. The matrix positions are spaced one particle diameter apart. The particles are randomly distributed into the matrix positions and using a statistical technique described in (4), the percentage laser power loss is expressed as the percentage occupied space in the matrix allowing for particles situated on top of each other and a correction for the area difference between square matrix and circular particle section.

Fig 10 illustrates the shadowing effect of the particles on the gaussian power intensity distribution of the beam. The total power loss is usually 10-20% for the range of cladding parameters used.

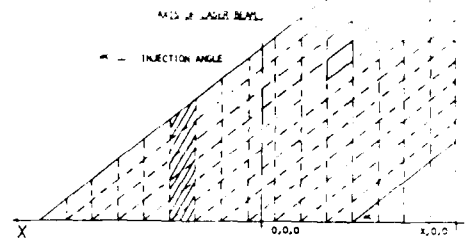


Fig 9. Powder cloud in relation to beam and substrate surface.

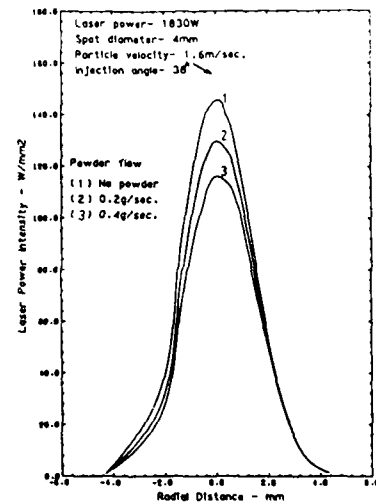


Fig 10. The shadowing effect of the particles on the gaussian intensity distribution of the beam.

#### PARTICLE TEMPERATURES - DELT (K,1)

The energy inputs to a particle travelling through the beam will be: directly from the laser, reflected energy from the substrate and reflected energy from other particles. As regards the latter, the multiple reflections in the powder cloud are modelled as a geometric progression

to calculate the fraction of the particle reflected energy entrapped in the powder cloud. The total power loss fraction is first calculated from  $R_{LOSS}(K,I)$ . This fraction defines the opacity of the powder cloud as a whole, and is used in the iterative progression to calculate the energy reflected energy by way of multiple reflections. A linear function varying from 0.0 at 1000 to a limiting value of 0.100 is used for the stainless steel particle surface reflectivity.

The traverse time across a typical element shown outlined in Fig 9, is calculated assuming the particle travels along a straight line inclined to the substrate at an angle equal to the injection angle. The power input to the particles in the vertical column containing this element will be  $RL(K,I) \times POWER(K,I)$ . The fraction absorbed is  $(1 - RF)$  where  $RF$  is the reduced reflectivity due to multiple reflections. The fraction absorbed from the beam reflected from the clad/substrate surface is also calculated in a similar manner. The energy input to a single particle in the element is calculated using the traverse time and assuming that the power input to the vertical column is shared equally by all the particles in that column. Although the particles at the top are likely to receive a higher proportion of the laser energy directly, the process is reversed for the reflected beam from the clad/substrate surface. The net effect is assumed to be an equal power sharing. The temperature rise is calculated assuming the particle to be of uniform temperature. A convective and a radiative loss is allowed for. The convective loss is based on an established empirical relationship (5,6). A conveying gas velocity of 4 m/s, relative to the particle is used. Both losses are based on an average of the temperature of the particle at the current position and the immediate previous position. The temperature of the current position is iterated to within 10% of the calculated current temperature using a trial and error loop. The progressive temperature rise of the particle is calculated until arrival on the clad/substrate surface. The model calculates the highest temperature of 70 micron stainless steel particles injected through a 5 mm beam of 1810W to be 1200K for a powder mass flow of 0.2 g/s, particle velocity of 1.6 m/s and injection angle of 38 deg.

#### HEAT BALANCE

The usual three dimensional finite difference heat balance equation is used (7,8,9), with two 'body convection' terms. A body convection term is used for the 'kinetic heat flow' in the substrate traverse direction, i.e. the 'x' direction. This is similar to that described in (3). The other term accounts for the powder injection process as follows:

$$\sum_{n=1}^N \frac{1}{\Delta t_n} \cdot \rho_p \cdot C_p \cdot \Delta t_n \cdot \Delta x_n$$

where

$$\Delta x_n = \frac{1}{2} (x_{n+1} + x_n) \cdot \Delta t_n$$

$$\Delta t_n = \frac{1}{2} (t_{n+1} + t_n) \cdot \Delta x_n$$

$t_n$  = temperature of a particle of the

size range, i.e.,

$n = 1$  particle size  $< 50 \mu m$

$n = 2$   $50 \mu m > \text{particle size} > 50 \mu m$

$n = k$

$\rho_p = \rho_M$  where  $\rho$  is the fraction of the particle size range in the powder mixture.  $M$  = powder mass injection per unit time to the grid point surface area.

Only one size range is considered in a weighted average size is used.

The term is added only for surface grid points which are molten. The term is zero for other points the particles would 'fall off' with negligible heat transfer.

A further assumption is that the particle melts and attains the grid point temperature within the grid point boundary. For some larger particles, this may not be true as ejection of particles from the molten pool has been observed.

The latent heat effects are accounted for using the 'temperature equivalent' method. If a grid point temperature reaches the melting point (i.e. an average between solidus and liquidus temperatures) then the temperature is reduced by the value  $L_f/C_p$ .

A convective and a radiative loss is allowed for all surface grid points.

The temperature dependence of the thermal conductivity is accounted by using linear functions (10,11,12) for the clad (stainless 316) and the substrate (mild steel EN3). materials, the values being calculated en route in the iteration process, and limited at 1650K.

The temperature dependence of the specific heat is allowed for the mild steel substrate. The specific heat of stainless 316 clad is assumed constant as variations with temperature are not significant.

Convergence is usually achieved after 500 iteration cycles. A low relaxation parameter coupled with a low convergence criteria is used.

# ALGORITHM AND RESULTS

The criteria which depict the quasi-steady state of the molten pool are: (Ref. Fig. 8)

(a) The temperature at point C1 (i.e. at the fully developed point of the bead) should be the clad melting point of the substrate melting point (whichever is higher). This is required for fusion to take place. The same applies to the temperature at point C2.

(b) The temperature at point C1 (i.e. the fully developed clad bead height) should be the melting point of the clad.

(c) The temperature of points after C1 in the positive x direction should be below the clad melting point if they are within the powder injection range. If this is not true, then the fully developed bead height will not be at point C1. The above argument should apply to all other points in the molten pool. However, only (x,0,0) points are considered as they are not affected by the 'step' in the grid.

(d) A continuous interface zone at the melting-point of the substrate to facilitate a fusion bond. This is obtained if (g) above is satisfied.

(e) The substrate surface points adjoining the clad bead boundary (including the elliptical boundary at the front end) should not be molten.

The temperature distribution is accepted as a solution if the above criteria are satisfied. In operating the model, the temperature distribution of the first estimated bead section profile is observed. The temperatures of the critical points of a first estimated bead profile are as follows:

Width = 2.5 mm    Height = 0.612 mm  
Temperature at C1 = 1487K  
C2 = 1603K  
C3 = 1575K

The above temperatures are seen to be too low, the melting point being 1650K. The limiting lengths of the heated zone, XR,YR,ZR are now adjusted if required. The program is re-run with a new width and height value until a satisfactory temperature distribution is obtained.

Temperature distribution for various widths and heights were studied. It was found that only a single combination of width and height satisfy all criteria concurrently. With experience, it is possible to arrive at this solution with 4-6 runs of the program.

Temperatures at the critical points of the accepted bead profile are as follows:

Width = 2.36 mm    Height = 0.669 mm

Temperature at C1 = 1650K  
C2 = 1650K  
C3 = 1644K

Temperature of the adjoining points in the positive x direction = 1644K (clad) substrate surface temperature = 1644K (clad boundary = 1644K)

Partial temperature distribution at certain transverse sections are listed below:

(i) Partial temperature (k) distribution at transverse section at x = 0.526 mm.

Y	0.000	0.262	0.524	0.787	1.049	1.311	2.296	mm
Z	0.000	-	-	-	-	-	-	-
0.149	-	-	-	-	-	-	-	-
0.297	-	-	-	-	-	-	-	-
0.446	-	-	-	-	-	-	-	-
0.595	1650	1644	-	-	-	-	-	-
0.743	1511	1508	1508	1469	1409	1329	998	Substrate
1.399	1008	1004	994	976	952	917	754	-

\* Temperature at C2

(ii) Partial temperature (k) distribution at transverse section at x = 1.292 mm.

Y	0.000	0.262	0.524	0.787	1.049	1.311	2.296	mm
Z	0.000	-	-	-	-	-	-	-
0.149	-	-	-	-	-	-	-	-
0.297	1856	1855	-	-	-	-	-	-
0.446	1818	1820	1853	1763	-	-	-	-
0.595	1730	1730	1735	1703	1649	-	-	-
0.743	1628	1627	1625	1612	1587	1562	1213	Substrate
1.399	1191	1189	1181	1166	1143	1112	913	-

\* Temperature at C3. The width is fully developed before the height.

(iii) Partial temperature (k) distribution at transverse section at x = 2.584 mm.

Y	0.000	0.262	0.524	0.787	1.049	1.311	2.296	mm
Z	0.000	1650	-	-	-	-	-	-
0.149	1604	1607	1548	-	-	-	-	-
0.297	1547	1543	1511	1471	-	-	-	-
0.446	1487	1482	1463	1441	-	-	-	-
0.595	1425	1421	1408	1391	1381	-	-	-
0.743	1362	1359	1349	1332	1307	1254	978	Substrate
1.399	1077	1074	1065	1050	1028	997	822	-

\* Temperature at C1.

The above solution is obtained for the following parameters: Laser power 1830W. Spot diameter 5 mm, Powder flow 0.2 g/s. Cladding speed 6.67 mm/s, Factor 'RM' 1.1, Factor 'RN' 0.26.

A clad bead of 2.24 mm width and 0.622 mm height is produced experimentally for the above process parameters. The error in the mass deposition rate is 14%.

The discrepancy between the computed and experimental results is due to the difference between the two sets of the experimental and the modelling process. As regards the modelling process, the two sets of the experimental results are compared with the computed results. The discrepancy between the two sets of the experimental results is due to the difference between the two sets of the experimental results.

#### OVERLAPPING OF SINGLE CLAD TRACKS TO OBTAIN A CLAD LAYER OF UNIFORM THICKNESS

The basic technique of producing uniform clad layers by laser cladding is by overlapping of single clad tracks. A model is developed to simulate this process. The model is based on the following experimental observations and assumptions.

- (a) The single track section profile is a segment of a circle.
- (b) The width of a multiple track layer of 'N' tracks is equal to  $W(N-1)x$  where 'x' is the transverse index and 'W' is the bead width.
- (c) Equal amount of clad metal is deposited each time a track is laid.

Using the above simple ideas, remarkable agreement with experimental data has been obtained. This is illustrated in Fig 11, where the computed development pattern of a clad layer is compared with the experimental. The simulation technique is shown in Fig 12 and a macrograph of a clad layer 'leading edge' is shown in inset Fig 11. The 'leading edge' (i.e. the distance before the clad thickness become uniform) has been substantially reduced by a higher initial overlap, the model being used to calculate the required parameters.

#### NOTES

1. The process parameters are required to laser clad material. The material is of A 304 stainless steel. The width of the track is 5.425mm.

2. The model is based on the following experimental observations and assumptions. (a) The single track section profile is a segment of a circle. (b) The width of a multiple track layer of 'N' tracks is equal to  $W(N-1)x$  where 'x' is the transverse index and 'W' is the bead width. (c) Equal amount of clad metal is deposited each time a track is laid. (d) The process parameters are required to laser clad material. The material is of A 304 stainless steel. The width of the track is 5.425mm. (e) The process parameters are required to laser clad material. The material is of A 304 stainless steel. The width of the track is 5.425mm. (f) The process parameters are required to laser clad material. The material is of A 304 stainless steel. The width of the track is 5.425mm. (g) The process parameters are required to laser clad material. The material is of A 304 stainless steel. The width of the track is 5.425mm. (h) The process parameters are required to laser clad material. The material is of A 304 stainless steel. The width of the track is 5.425mm. (i) The process parameters are required to laser clad material. The material is of A 304 stainless steel. The width of the track is 5.425mm. (j) The process parameters are required to laser clad material. The material is of A 304 stainless steel. The width of the track is 5.425mm. (k) The process parameters are required to laser clad material. The material is of A 304 stainless steel. The width of the track is 5.425mm. (l) The process parameters are required to laser clad material. The material is of A 304 stainless steel. The width of the track is 5.425mm. (m) The process parameters are required to laser clad material. The material is of A 304 stainless steel. The width of the track is 5.425mm. (n) The process parameters are required to laser clad material. The material is of A 304 stainless steel. The width of the track is 5.425mm. (o) The process parameters are required to laser clad material. The material is of A 304 stainless steel. The width of the track is 5.425mm. (p) The process parameters are required to laser clad material. The material is of A 304 stainless steel. The width of the track is 5.425mm. (q) The process parameters are required to laser clad material. The material is of A 304 stainless steel. The width of the track is 5.425mm. (r) The process parameters are required to laser clad material. The material is of A 304 stainless steel. The width of the track is 5.425mm. (s) The process parameters are required to laser clad material. The material is of A 304 stainless steel. The width of the track is 5.425mm. (t) The process parameters are required to laser clad material. The material is of A 304 stainless steel. The width of the track is 5.425mm. (u) The process parameters are required to laser clad material. The material is of A 304 stainless steel. The width of the track is 5.425mm. (v) The process parameters are required to laser clad material. The material is of A 304 stainless steel. The width of the track is 5.425mm. (w) The process parameters are required to laser clad material. The material is of A 304 stainless steel. The width of the track is 5.425mm. (x) The process parameters are required to laser clad material. The material is of A 304 stainless steel. The width of the track is 5.425mm. (y) The process parameters are required to laser clad material. The material is of A 304 stainless steel. The width of the track is 5.425mm. (z) The process parameters are required to laser clad material. The material is of A 304 stainless steel. The width of the track is 5.425mm.

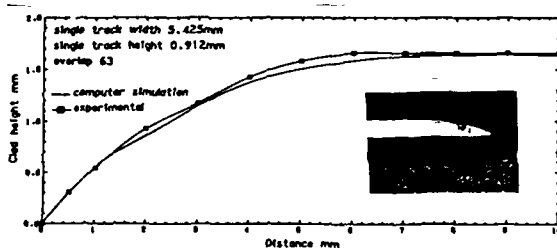


Fig 11. Development pattern of a clad layer.





END

DATE  
FILMED

7 - 84

DTIC

END

DATE  
FILMED

7 - 84

DTIC